Pergamon

Int. J. Impact Engng Vol. 16, No. 2, pp. 293–320, 1995
Elsevier Science Ltd
Printed in Great Britain

0734-743X(94)00041-7

0734-743X/95 $9.50 + 0.00

THE INFLUENCE OF PLATE HARDNESS ON THE BALLISTIC PENETRATION OF THICK STEEL PLATES

S. N. DIKSHIT,† V. V. KUTUMBARAO‡ and G. SUNDARARAJAN†

†Defence Metallurgical Research Laboratory, Kanchanbagh, Hyderabad-500 258, India and
‡Department of Metallurgy, Banaras Hindu University, Varanasi, 221005, India

(*Received* 2 *November* 1993; *in revised form* 15 *July* 1994)

Summary—This investigation describes and analyses the experimental results pertinent to the penetration of steel plates of varying hardness in the range HV295–HV520 and of thickness 20 and 80 mm by ogive-shaped 20-mm-diameter projectiles over the velocity range 300–800 m s^{-1}. All the tests were carried out at normal impact angle, i.e. zero obliquity. The experimental results presented include the variation of depth of penetration, crater volume, lip height, bulge height and diameter, plugged length and diameter and specific energy absorption capacity with impact velocity for tests on each plate of a given hardness and thickness. Selected data and observations relating to the plastic zone size and shape surrounding the penetrating projectile, incidence and extent of adiabatic shear band (ASB) formation and plate spalling have also been presented. These experimental data have been interpreted in terms of the appropriate penetration mechanisms like ductile hole formation, bulging followed by star cracking, ASB-induced shear plugging, etc., and also by making use of the fact that the projectile undergoes substantial deformation when penetrating the harder plates (HV450 and HV520). It is also demonstrated that the resistance to penetration and hence the mechanism of penetration is very much dependent on whether the penetration occurs under plane strain or plane stress conditions. For example, ASB-induced plugging occurs only under plane stress conditions while projectle deformation is dominant only under plane strain conditions even in harder plates.

1. INTRODUCTION

The resistance of metallic materials to ballistic penetration depends on a number of parameters. These parameters can be broadly classified as projectile-related (projectile size, shape, density and hardness), impact-related (impact velocity and angle) and target plate-related (hardness/strength, ductility, microstructure and plate thickness). The present paper is primarily concerned with the influence of target plate material properties, especially hardness, on its ballistic resistance.

A perusal of the open literature in the area of ballistic penetration of metallic plates at ordnance velocities indicates that a majority of the work reported is for thin plates ($T/D < 1$, T = plate thickness; D = projectile diameter). For thin plates, extensive literature pertaining to the experimental data and also on modelling of the penetration process [1–19] is available. Many of these studies have also utilized small-calibre projectiles. However, for thick plates ($T/D \geqslant 1$), the available experimental data are quite limited [2,20–24], even though a number of analytical and numerical models valid for thick plates have been proposed in the literature [2–4,25–28].

Literature data on the effect of plate hardness on ballistic performance of steels are very limited and even these data pertain to thin plates [29,30]. Such data indicate that as the hardness of the plate is increased so does the ballistic peformance up to a certain hardness level. Beyond this hardness, the ballistic performance of steel actually decreases with increasing hardness due to shear plugging induced by the formation and propagation of adiabatic shear bands. If the hardness of the steel plate is increased further to approach that of the projectile, its ballistic performance improves again due to projectile shatter/deformation.

In the case of penetration of thick plates (20 and 80 mm) by large calibre projectiles (20 mm diameter), no systematic data is available in the open literature on the effect of

plate hardness on its ballistic performance. In an earlier study [24], the influence of plate thickness (20, 40 and 80 mm) on ballistic performance with a large calibre projectile (20 mm diameter) was investigated and it was concluded that the penetration under plane strain and plane stress conditions had entirely different characteristics. It was also noted that the transition from plane strain to plane stress conditions occurs when the plastic zone ahead of the penetrating projectile just impinges on the backface of the plate. Thus, all of the penetration of thin plates ($T/D \ll 1$) occurs under plane stress conditions, while for thick plates ($T/D \gg 1$) it is all under plane strain. At this juncture it should be stated that the terms plane strain and plane stress have been defined rather loosely by us to imply confined/constrained and unconstrained plastic flow, respectively. In the case of constrained plastic flow, the stress state is always one of plane strain. However, in the case of unconstrained plastic flow, the stress state need not be one of plane stress especially if the plate thickness is sufficiently large to support through the thickness stress. In the present experiments, such a situation did not arise.

The above discussion indicates that since much of the literature data on the effect of plate hardness on ballistic performance is with thin plates, they represent hardness effects under plane stress conditions. In the present study, the projectile–plane combination chosen is such that the T/D ratio is 1 for 20 mm plate and 4 for 80 mm plate. Hence, ballistic testing of 20 and 80 mm plates with a range of hardness should provide valuable information on the influence of the stress state (i.e. plane strain or plane stress) during penetration on the "hardness effect". In addition, the importance and relative dominance of various penetration mechanisms like ductile hole formation, bulging followed by star cracking, shear plugging and also the extent of projectile deformation and fracture under plane strain and plane stress conditions can be compared and contrasted as a result of such a study.

Therefore, the major objective of the present investigation is to charactrize the penetration of 20-mm-diameter, ogive-shaped, steel projectiles into steel plates with hardness values in the range HV295–HV520 and of thickness 20 and 80 mm. For each plate of a given hardness and thickness, a series of tests, all at sub-ballistic limit velocities, were carried out to characterize the changing nature of the resistance to penetration offered by the plate material as a function of penetrated distance. These data, in conjunction with the other experimental data and observations related to the plastic zone size, extent of bulge on the rear side of the plate, incidence of adiabatic shear band and plug formation, have been used to clarify the penetration mechanisms involved.

2. EXPERIMENTAL DETAILS

2.1. *Plate material*

Rolled homogeneous armous (RHA) plates of thicknesses 20 and 80 mm were used as the target. The steel plates, of low alloy steel composition, were used in the as-received (AR) as well as in the quenched and tempered (QT) conditions. The heat-treatment details and the corresponding Vickers hardness (HV) values at 30 kg load are provided in Table 1. Thus, 20-mm-thick plates of hadnesses HV300, 350, 440 and 520 and 80-mm-thick plates of hardnesses HV295, 440 and 520 were tested for ballistic response. However, some plates of hardness HV470 were also ballistically tested, just to examine the impact craters formed.

Tensile specimens were taken from steel plates of different hardness levels and the tensile tests were carried out on an Instron machine at a crosshead speed of $2\,\text{mm}\,\text{min}^{-1}$ corresponding to an initial strain rate of $1.33 \times 10^{-3}\,\text{s}^{-1}$. The 0.2% offset yield strength (σ_{ys}), the ultimate tensile strength (σ_{UTS}), the uniform strain (ε_u) and the fracture strain (ε_f) were obtained for steel samples of each hardness from the load–sample extension curves obtained from tensile testing. The variation of the above parameters with hardness (HV) is illustrated in Fig. 1. As expected, σ_{ys} and σ_{UTS} increase with increasing hardness while ε_u and ε_f show the opposite trend.

The load–extension curves were converted to true plastic stress (σ)–true plastic strain (ε)

Table 1. Test material details

S.I. No.	Condition	Plate thickness (mm)	Vickers Hardness (HV)
1.	Hot rolled, as received condition (AR)	20	350±10
2.	Hot rolled, as received condition (AR)	80	300±15
3.	AR±quenched in oil+tempered at 350°C for 1 h ($\frac{1}{2}$ h for 20 mm)	20, 80	520±15
4.	AR+quenched in oil+tempered at 465°C for 1 h ($\frac{1}{2}$ h for 20 mm)	20, 80	440±10
5.	AR+quenched in oil+tempered at 650°C for $\frac{1}{2}$ h)	20	300±10

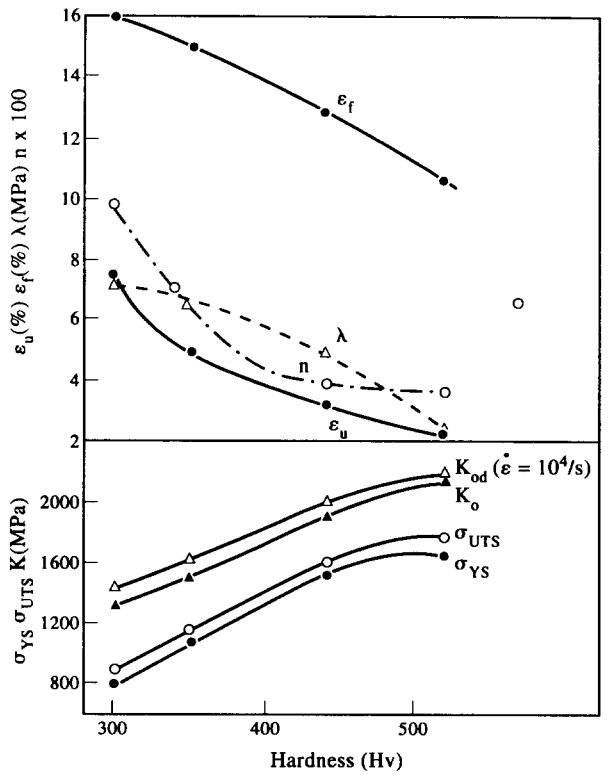

Fig. 1. The variation of both the strength and ductility parameters of the low alloy steel with its hardness.

curves and further fitted to a power-law strain-hardening equation of the form

$$\sigma = \text{flow stress} = K_0 \varepsilon^n. \tag{1}$$

In Eqn (1), K_0 is the strength coefficient and n is the strain-hardening exponent. The variation of the best-fit values of K_0 and n with hardness are also illustrated in Fig. 1. While n decreases with increasing hardness, K_0, being a strength parameter, shows the opposite behaviour.

In Eqn (1), the parameter K_0 is usually found to be strain-rate sensitive. The dependence of K_0 on strain rate ($\dot{\varepsilon}$) is usally expressed in the form [22,23].

$$K_{0d} = K_0 + \lambda \ln \dot{\varepsilon}/\dot{\varepsilon}_0. \tag{2}$$

In Eqn (2), K_{0d} is the dynamic value of K_0 at a strain rate of $\dot{\varepsilon}$, $\dot{\varepsilon}_0$ is the strain rate ($=1.33 \times 10^3\ s^{-1}$) at which the tensile tests were carried out and λ is usually defined as the strain-rate sensitivity parameter. In the present case, λ values were obtained for steel plates of each hardness, by carrying out an additional tensile test at a strain rate of $1.33 \times 10^{-1}\ s^{-1}$ and by comparing the K_0 values obtained at the two strain rates. The values of λ so estimated are also presented in Fig. 1. λ is seen to decrease with increasing hardness. The values of K_{0d}, calculated using Eqn (2) and Fig. 1 (for λ), for a dynamic strain rate of $10^4\ s^{-1}$ appropriate to the plastic deformation that occurs during ballistic penetration are also given in Fig. 1. It is clear from Fig. 1 that K_{0d} is only marginally higher than K_0.

2.2. *Projectile*

A steel cylinder with an ogive nose, of diameter 20 mm (beyond the nose region) and a mass of 110 g, was used as the projectile in all the penetration tests reported in this paper. The hardness of the projectile, as measured on the sectioned surfaces at the projectile, was about HV600 (at 30 kg load). Thus, the projectile was harder than even the hardest steel plate used (HV520 $\pm$ 10). The three-dimensional profile of the projectile was determined and hence the volume of the projectile as a function of distance along its cylindrical axis from its nose tip. These data have been presented in an earlier paper (Fig. 1 of Ref. [24]).

2.3. *Ballistic test details*

All the balistic tests were conducted at zero obliquity, i.e. the projectile path was normal to the plane of the target plate. The sizes of the plates used were approximately 450 x 450 mm. During the tests, the steel plates were clamped firmly to the target holder already positioned for an attack angle of 0° and the projectiles were fired from a gun kept at a distance of about 30 m from the target plate. Two screens of aluminium foil (0.01 mm thick) placed in the path of the projectile at a known distance apart, were used to measure the velocity (V) of the projectile before it impacted the steel plate. The accuracy of velocity measurement was within $\pm 5\ m\ s^{-1}$.

Six to eight shots were impacted on each plate. The impact velocity was varied by varying the charge mass of the propellant. It was also ensured that the centre-to-centre distance between any two impact craters on the plate was at least four times the diameter of the projectile, while the distance from the impact centre to the edge of the plate was at least twice the projectile diameter. Wherever these distance criteria were not met, the craters were not considered for further analysis.

2.4. *Post-impact examination*

After the ballistic tests, each impact crater was examined in great detail. First, the impact craters on the target plate were photographed both on the entry and exit side. The various parameters that were measured on the impact crater are illustrated in Figs 2a and b. Figure 2a represents a sectioned view of a typical crater formed on the lower hardness steel plates by ductile hole penetration followed by bulging. In contrast, Fig. 2b illustrates a sectioned view of the typical crater formed on high hardness steel plates by ductile hole formation followed by plugging. In both the cases, the depth of penetration (X_p) was measured using a three-dimension measuring machine. The entry hole diameter (D_e), defined as the diameter on the original plate top surface plane, was measured using an electronic digital caliper. The crater volume (U) was computed by filling the crater up to the original target plate level with plasticine of known density. The lip height (H), the bulge height (H_b), the bulge diameter (D_b), plug diameter (D_p) and the entry hole diameter (D_e) (Figs 2a and b) were measured using a specially designed, portable stand with four-point support and fitted with a level meter, a mobile pointer and a length scale of resolution ± 0.25 mm. The accuracy of measurements were always less than ± 0.1 mm with respect to X_p and D_e, while it was about ± 0.25 mm for measurements of H, H_b, D_b and D_p.

After making the above measurements, selected impact craters were sectioned along their diameter to result in a sectioned surface as shown in Figs 2a and b. This sectioned surface was then ground and polished in emery paper up to 600 grit. Both microhardness (200 g

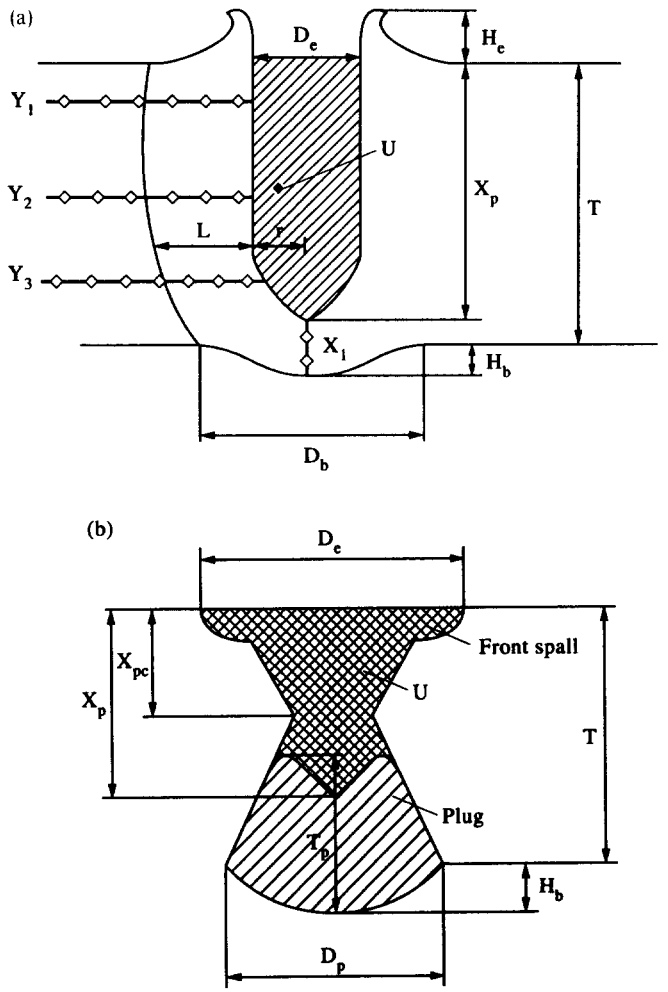

Fig. 2. A schematic of the sectioned view of the impact craters formed on (a) low hardness and (b) high hardness plates. The various parameters of interest are illustrated in each figure.

load, Vickers indenter) and macrohardness (30 kg load, Vickers indenter) measurements were performed on the sectioned surface. A series of hardness measurements, at regular intervals were taken on the sectioned surface along the lines Y_1, Y_2, Y_3 and X_1 as shown in Fig. 2. Using this information, the hardness–distance profiles could be determined, and in turn the distance up to which the plastic zone extends from the side walls of the impact crater (i.e. distance L marked in Fig. 2a) could be estimated.

These sectioned surfaces of the impact craters were then etched in nital and examined in an optical microscope for the presence of white etching-transformed or untransformed adiabatic shear bands (ASBs).

3. EXPERIMENTAL RESULTS

3.1. *Ballistic penetration of 20-mm plates*

(a) Appearance of impacted plates. The impacted steel plates of 20 mm thickness and hardness HV300, 350, 440 and 520 were examined for assessing the nature and mode of deformation of the plate material. Figures 3a–f illustrate the typical entry and exit features of the craters (or holes), formed on 20-mm plates of hardness HV300 (a,b; $V = 629\ \mathrm{m\ s^{-1}}$), HV400 (c,d; $V = 603\ \mathrm{m\ s^{-1}}$) and HV520 (e,f; $V = 540\ \mathrm{m\ s^{-1}}$) respectively. On the entry side, substantial lip formation all around the periphery of the impact crater can be observed in

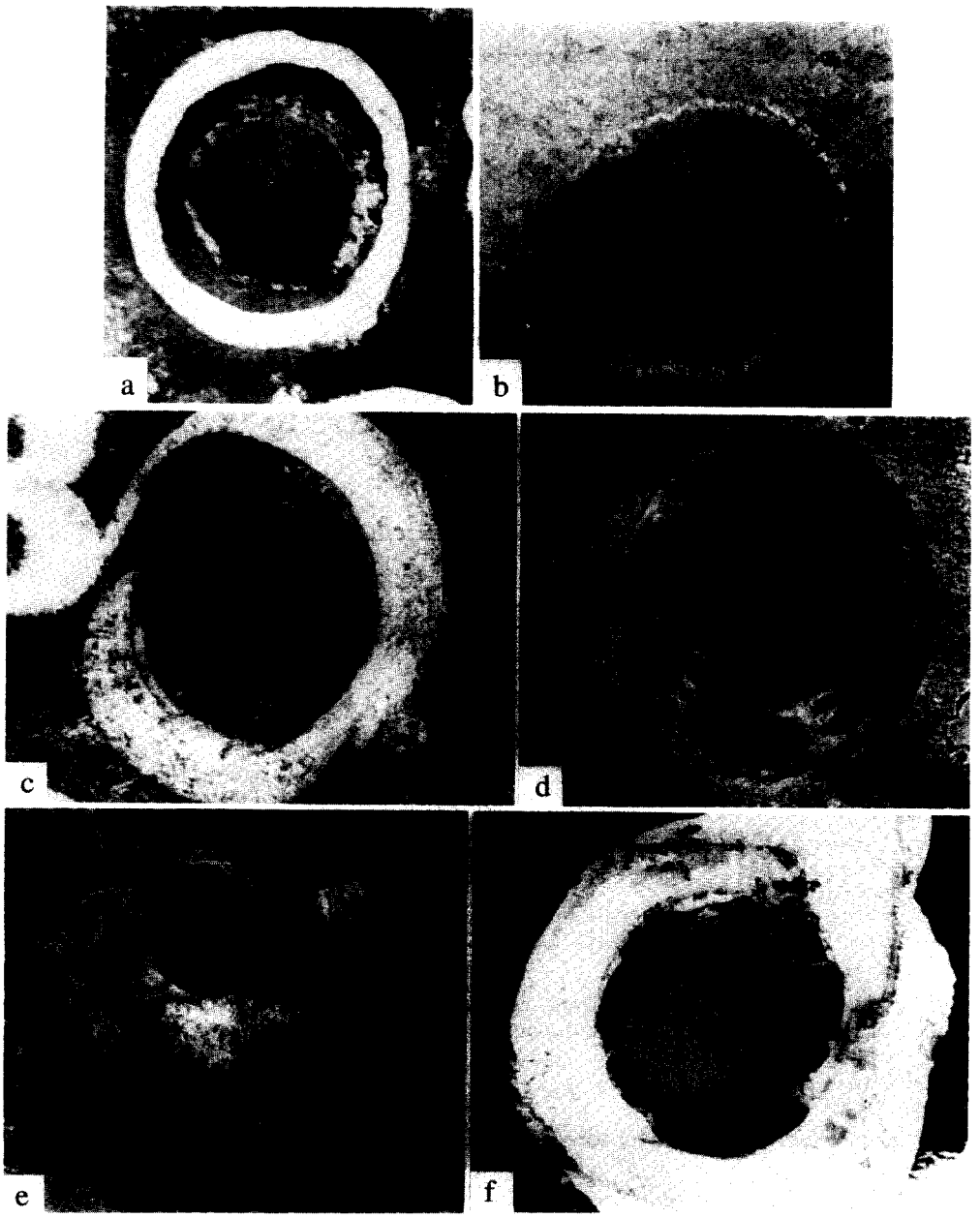

Fig. 3. The typical appearance of the craters formed on 20 mm plates of hardness HV300 (a, b; $V = 629\ m\ s^{-1}$), HV440 (c,d; $V = 603\ m\ s^{-1}$) and HV520 (e,f; $V = 540\ m\ s^{-1}$). (a,c,e) represent the entry side and (b,d,f) the exit side.

HV300 plate (Fig. 3a). In contrast, in HV400 and HV520 plates, lips are not seen on the entry side of the craters (Figs 3c and e). However, the presence of a thin fractured zone all along the periphery of the crater points to the fact that though the lip formed during the penetration process, it also got fractured during the same penetration process. On the exit side, in the case of HV300 plate, the formation of a bulge and its subsequent perforation by star crack formation can be noticed (Fig. 3b). In the case of HV440 and HV520 plates, complete perforation has occurred by plugging (Figs 3d and f). However, the large plugged area, especially in the HV520 plate, would suggest that discing features are also present. In the present paper, the generic term "plugging" will be used to mean both plugging and discing mechanisms since both are induced by ASBs in the current set of experiments.

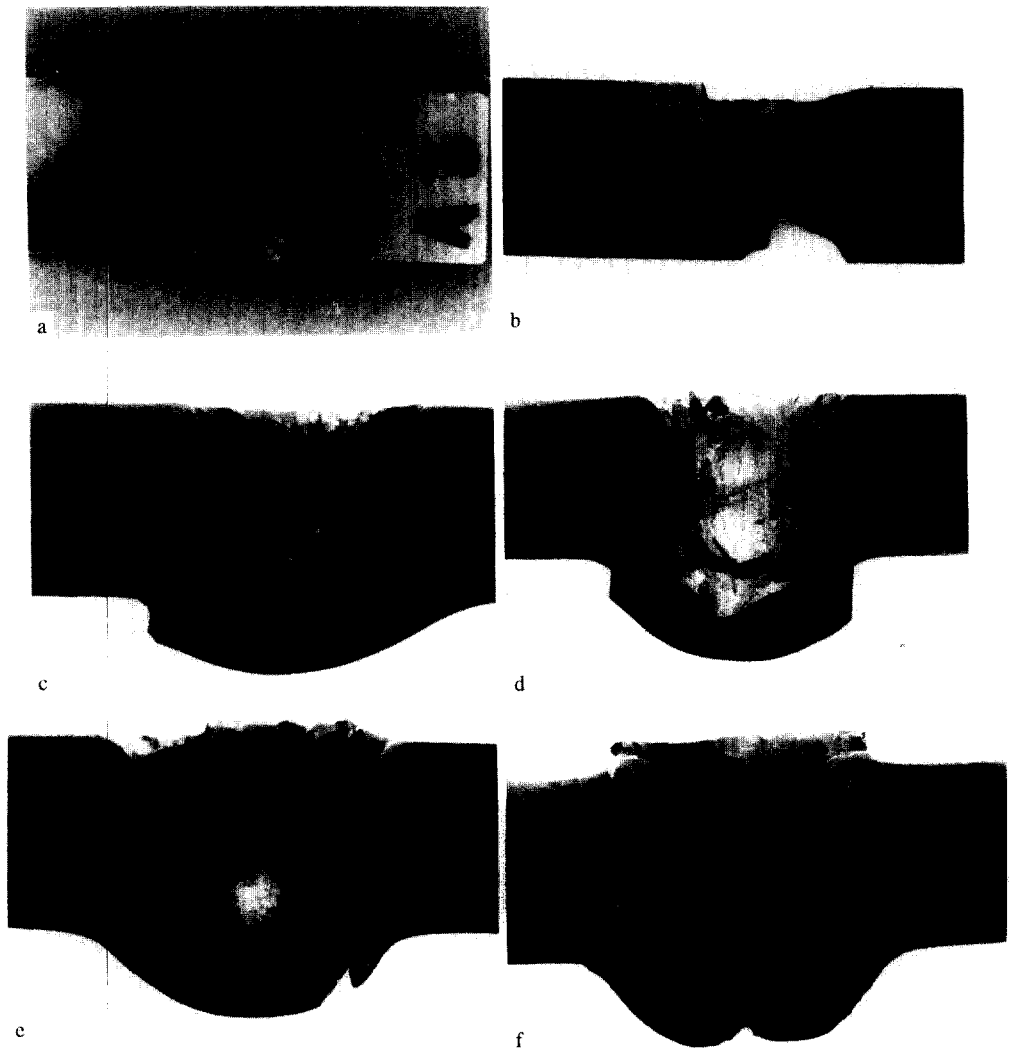

Fig. 4. Sectioned views of the impact craters formed on 20-mm-thick plates (a, HV520, $V = 394\ m\ s^{-1}$; b, HV520, $434\ m\ s^{-1}$; c, HV470, $V = 520\ m\ s^{-1}$; d, HV470, $V = 537\ m\ s^{-1}$; e, HV390, $V = 580\ m\ s^{-1}$; f, HV350, $V = 580\ m\ s^{-1}$).

However, as noted by Woodward [31], each of these two mechanisms has its own distinctive features.

The sectioned views of the impact craters formed on 20-mm-thick steel plates of various hardness levels are presented in Fig. 4. Figures 4a and b represent the craters formed on a HV520 plate at impact velocities of 394 and 434 m s^{-1} respectively. At $V = 394$, the crater has a smooth appearance and backside bulging can be seen. However, as will be shown subsequently, even at this velocity ASBs have formed around the crater. However, they have not propagated sufficiently to cause plugging. At $V = 434\ m\ s^{-1}$, the crater has a remarkably different appearance (Fig. 4b) even though this velocity is higher by only $40\ m\ s^{-1}$ compared with Fig. 4a. The back side has plugged completely because of the through thickness crack propagation along the ASBs. Even the crater walls appear fragmented. The fragments are formed by the intersection of cracks formed along the ASBs.

The sectioned views of the craters formed on HV470 ($V = 502\ m\ s^{-1}$) and HV440 ($V = 537\ m\ s^{-1}$) steel plates are illustrated in Figs 4c and d respectively. Both the craters are characterized by a circumferential spall on the entry side and by extensive cracking (along ASBs) on the exit side. In Fig. 4c, the initial stages of plug formation can be observed while in Fig. 4d, the plug has just formed and has been already pushed by a few millimetres by the projectile.

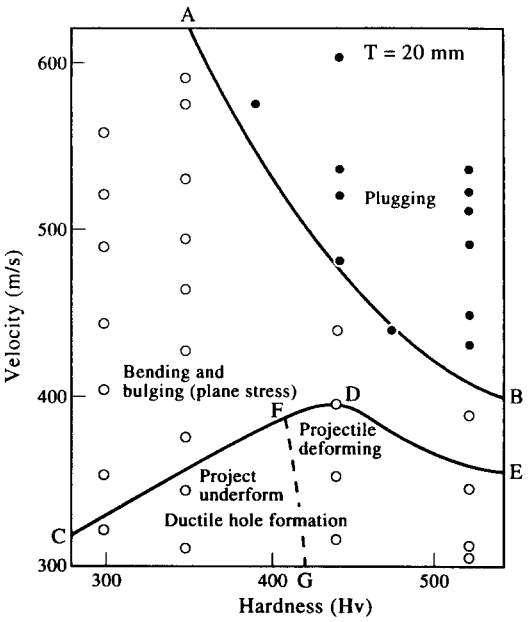

Fig. 5. A velocity–hardness ballistic performance map for 20-mm plates, indicating the dominance of the various mechanisms of ballistic penetration. The solid and dashed line demarcate the regions while the circles represent an experimental data point. Filled circles indicate plugging, while unfilled circles correspond to bulging.

Figures 4e and f show the craters formed on HV390 and HV350 steel plates. In both cases, extensive bulging of the back side of the plates can be noted. In the HV350 plate, while the lips can be observed along the periphery of the hole on the entry side, it has been removed by spalling on HV390 plate.

Another interesting aspect which can be noted from Fig. 4 pertains to projectile deformation during penetration. At one extreme, in the case of the craters formed on HV520 plates (Figs 4a and b), the crater profiles are more rounded and flattened at their tip, pointing to projectile deformation. In contrast, at the other extreme, the profiles of the craters formed on HV350 (see Fig. 4f) and HV300 plates faithfully simulate that of the projectile, indicating negligible projectile deformation during penetration. This aspect will be considered in greater detail in a subsequent section.

On the basis of the examination of the impact craters formed on steel plates of different hardness and over a range of velocities, it is now possible to define approximately the minimum velocity required for plugging failure as a function of plate hardness (for a 20-mm-thick plate). In Fig. 5, which represents a velocity–hardness space, the velocity–hardness combinations which resulted in plugging are indicated as filled circles, while those combinations which did not cause plugging are represented as open circles. The boundary line between the plugging and non-plugging regime is also indicated in Fig. 5 (curve AB). As expected, the minimum velocity for plugging increases with decreasing hardness of the plate. At HV300 and 350, plugging was not observed within the velocity range (300–600 m s^{-1}) used in the present experiment. The other features contained in Fig. 5 will be described in the subsequent sections.

(b) Adiabatic shear bands. It is generally accepted that plugging occurs by the cracking of the material along the ASBs. To confirm this point, the sectioned impact crater formed on HV520 plate at an impact velocity of 394 m s^{-1} (Fig. 4a) was examined in greater detail. The craters formed on the same plate but at higher velocities were found unsuitable since they already exhibited cracks which masked the ASBs. Figure 6 shows higher magnification optical micrographs of the regions around the impact crater bottom. It can be noted from Fig. 6b that the crater bottom is essentially interspersed with criss-crossing ASBs (seen as the white bands). Some of the ASBs contain cracks. In addition to these ASBs which were

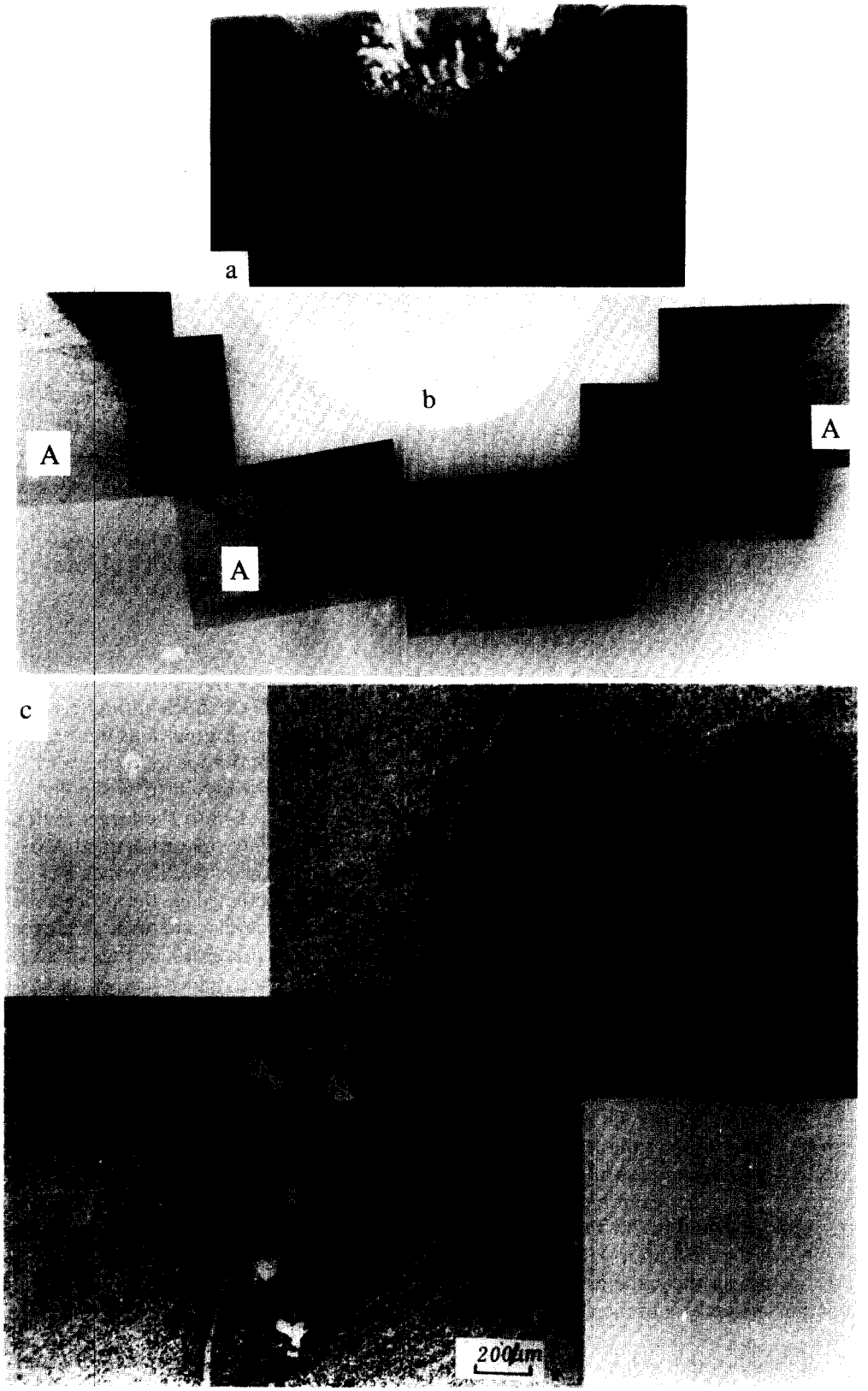

Fig. 6. (a) The sectioned view of the impact crater formed on 20-mm plate of hardness HV520 at $V = 394\ \mathrm{m\ s^{-1}}$; (b) and (c) provide higher magnification views of the selected areas of the crater.

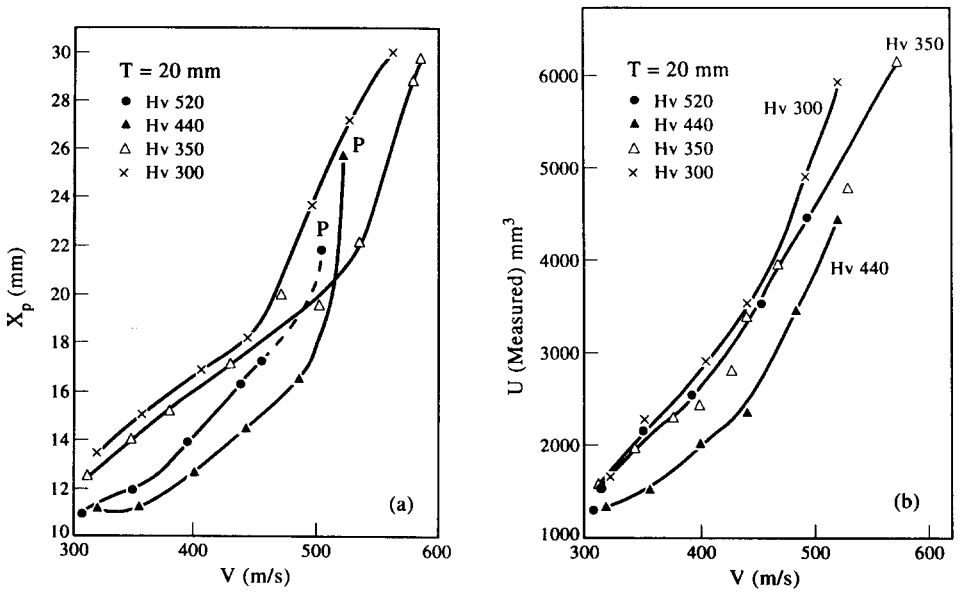

Fig. 7. The variation of (a) depth of crater (X_p) and (b) measured crater volume (U) with impact velocity in 20-mm plates. The data corresponding to HV300, HV350, HV440 and HV520 plates are indicated by crosses, unfilled triangles, filled triangles and filled circles, respectively.

confined to only a depth of 0.2–0.3 mm from the crater bottom, a few ASBs (as in location A of Fig. 6b) were observed penetrating deep into the plate. These ASBs ultimately cause plugging. A closer view of one of these long ASBs is presented in Fig. 6c. This figure shows the merger of two ASBs into one. The width of the shear band appears to be very low and in the region of 10 μm. To conclude, Fig. 6 confirms the widely held viewpoint that plugging requires first the initiation and propagation of an ASB into the target material ahead of the crater bottom followed by crack propagation along the just-formed ASB.

(c) Penetration depth and volume. The depth up to which the projectile penetrates (X_p; Fig. 2) into the steel plate and the volume of the crater (U) created in the process were experimentally measured on the plates of various hardness levels and over a range of impact velocities. The results obtained on 20-mm plates are presented in Figs 7a and b. The depth of penetration (X_p) increases with increasing impact velocity at all hardness levels. For a given impact velocity lower than about 500 m s^{-1}, the depth of penetration (X_p) decreases with increasing hardness up to HV440. However, the HV520 steel exhibits a higher depth of penetration than HV440 steel. In all the steels, depth of penetration has exceeded the nominal thickness of the plate (= 20 mm) because of the bulging of the backside of the plate. In the HV300 and 350 steels, the onset of bulging is also indicated by the increase in the slope of the X_p–V curves at higher impact velocities. In the case of HV440 and 520 steels, the increase in the value of X_p with V is quite dramatic at the higher velocities leading to X_p values even higher than that obtained in HV350 steels.

As indicated in Fig. 7b, the volume of the craters (U) also decreases with increasing hardness of the steel up to HV440. The crater volumes (U) obtained in the case of HV520 steels are nearly the same as those obtained with HV350 steels. The effect of increasing the impact velocity is to increase the crater volume irrespective of the hardness of the steel plate.

Both Figs 7a and b indicate that the crater volume and depth of penetration are generally higher for the harder HV520 steel as compared with the HV440 steel. However, there is a definite indication that at very low impact velocities (< 320 m s^{-1}), U and X_p values are comparable or even lower for HV520 steel as compared with HV440 steel.

(d) Bulge profile. As noted earlier (see Fig. 2), a bulge is formed on the rear side of the plate once the plastic zone ahead of the penetrating projectile impinges on the rear face

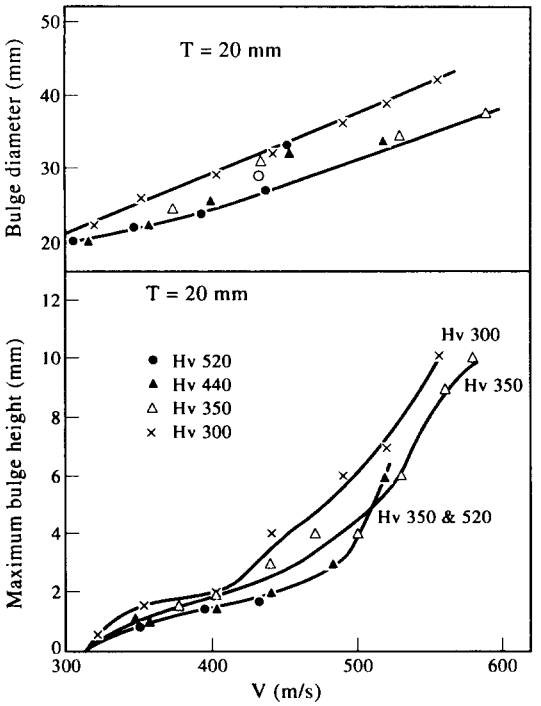

Fig. 8. The variation of maximum bulge height (H_b; Fig. 2a) and bulge diameter (D_b; Fig. 2a) with impact velocity in a 20-mm plate of hardness HV300 (crosses), HV350 (unfilled triangles), HV440 (filled triangles) and HV520 (filled circle).

of the plate. The variation of the maximum bulge height (H_b; Fig. 2) and bulge diameter (D_b; Fig. 2) as a function of impact velocity is presented in Fig. 8 for 20-mm-thick steel plates of hardness HV300, 350, 440 and 520. Noticeable bulge on the backside occurs at velocities as low as 350 m s^{-1}. In the case of HV300 and 350 plates, extensive bulging occurs and the bulge height (H_b) reaches values as high as 10 mm before perforation occurs by the formation of star cracks (see Fig. 3b). In contrast, the bulge heights are lower in the HV440 and HV520 steels. However, in these steels, bulge occurs to a limited extent (up to 6 mm height in HV440 and up to 2 mm height in HV520) before failure occurs by plugging (Fig. 3). The bulge diameter, however, does not show any substantial effect due to the plate hardness. Rather, the bulge diameter continuously increases with increasing impact velocity at all hardness levels.

(e) Nature of the plug. It has already been noted (Fig. 5) that the HV440 and HV520 steels failed by plugging beyond a certain velocity. The plugging mode of failure intervened only after a certain amount of penetration (by ductile hole formation) had occurred. The plugged region can be easily identified by examining the hole formed upon the perforation of the plate by the projectile since it has a smooth, shiny appearance. Thus, the penetration depth at which plugging initiated (X_{pc}, see Fig. 2b) can be easily estimated and hence the plug thickness ($T_p = T + H_b - X_{pc}$). Similarly, the diameter of the hole on the exit side (though non-circular) will provide information on the diameter of the plug. The values of X_{pc} are provided in Table 2.

(f) The extent of plastic zone. As described in Section 2.4, hardness profiles were obtained on sectioned surfaces perpendicular to the direction of motion of the projectile (see Fig. 2) to estimate the plastic zone size. The experimental hardness–distance profiles obtained around the impact craters formed on 20-mm plates of hardness HV350 ($V = 377$ and 468 m s^{-1}), HV440 ($V = 537$ m s^{-1}) and HV520 ($V = 538$ m s^{-1}) are presented in Figs 9a, b and c, respectively. Hardness profiles were obtained at distances of 3 mm (filled circles), 10 mm (filled triangles) and 17.5 mm (filled rectangles) from the original, top surface of the plate in the case of HV440 and HV520 steels, while in the HV350 steel the profiles were

Table 2. Details regarding plugging in HV440 and 520 steels ($T = 20$ mm)

Hardness (HV)	*Velocity (m s^{-1})*	X_{pc} *(mm)*	X_{pc}/T
440	561.8	12.0	0.60
	575.0	13.0	0.65
470	496.0	12.2	0.61
	527.0	11.4	0.57
520	472.0	10.0	0.50
	493.5	11.0	0.55
	526.6	12.0	0.60

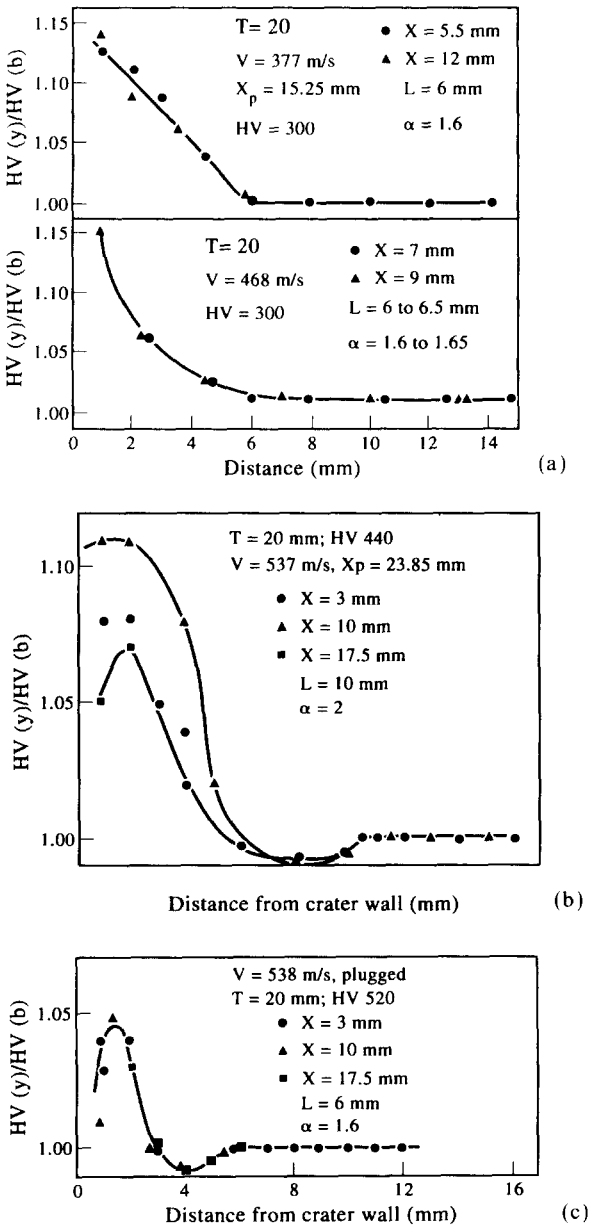

Fig. 9. The variation of hardness (HV(y)) normalized by bulk hardness (HV(b)) as a function of distance from the crater wall (i.e. along lines Y_1, Y_2, etc. in Fig. 2a) in 20-mm plates. X represents the distance of the line along which the hardness profile was obtained from the original top surface of the plate (a, $V = 377$ and 468 m s^{-1}, HV = 350; b, $V = 537$ m s^{-1}, HV = 440; c, $V = 538$ m s^{-1}, HV = 520).

obtained at distances of 5.5, 7, 9 and 12 mm from the top surface of the plate. All the hardness values reported in Fig. 9 have been normalized by the base hardness of the plate (i.e. 350, 440 or 520 kg mm^{-2}).

The normalized hardness value is observed to increase continuously with decreasing distance from the crater wall, at both the impact velocities ($V=377$ and 468 m s^{-1}), in the case of steel plate of hardness HV300 (Fig. 9a). Since HV300 steel has the ability to work harden to a significant degree (see Fig. 1), the presence of a steep hardness gradient is actually the reflection of a strong plastic strain gradient within the plastic zone. In the case of HV400 and HV520 steels, the normalized hardness values increase with decreasing distance from the crater wall only up to a distance of about 2 mm. At distances below 2 mm from the crater wall, the normalized hardness value starts decreasing substantially as the crater wall is approached. The heat generated in the target steel plate during plastic flow around the penetrating projectile and the resulting temperature rise can reduce the hardness of the plate if the temperature so generated exceeds the tempering temperature of the steel. Thus, in our opinion, in HV440 and HV520 steels the increase in hardness due to work hardening is more than off-set by the temperature-induced softening at distances very close to the crater wall (wherein the temperature rise is also maximum), resulting in the observed soft zone. In the case of HV300 steel, the fact that its original tempering temperature is high ($\simeq 650$°C) compared with that used for HV440 ($\simeq 465^0$C) and HV520 ($\simeq 650$°C) steels, coupled with the fact with the lower strength of HV300 steel as compared with HV440 and HV520 steels will also result in a lower heat generation and hence a reduced temperature rise, can explain the absence of the soft zone near the crater wall.

In addition to the soft zone present near the crater wall, the hardness profiles of HV440 and 520 steels (Figs 9b and c) also indicate the presence of yet another low hardness zone at distances of about 8 and 4 mm from the crater wall. The reasons for the formation of these secondary soft zones are not yet clear.

It is also clear from Fig. 9 that the hardness attains the base value at distances of about 6.0–6.5 mm, 10 mm and 6 mm in the case of HV350, HV440 and HV520 plates, respectively. These distances are defined as L in Fig. 2. However, it is to be noted that even the volume of material which has been displaced to form the crater has been plastically deformed first. Thus, the plastic zone size should actually equal $L+r$, where r is the radius of the projectle. If α is defined as $(L+r)/r$, then α equals 1.60–1.65, 2.0 and 1.6 for HV350, HV440 and 520 plates respectively.

(g) Cumulative specific energy absorbed. The cumulative specific energy (E_{sc}) absorbed by the plate during projectile penetration is given by

$$E_{sc}=0.5mv^2/U. \tag{3}$$

In Eqn (3), U is the volume of the crater formed in the target plate when it is impacted by a projectile of mass m at a velocity V. Equation (3) is valid only at velocities below the ballistic limit (since it assumes zero residual velocity) and E_{sc} in Eqn (3) represents the average resistance offered by the plate to projectile penetration.

In Eqn (3), the crater volume (U) can be obtained in two ways. The first method is to obtain it experimentally (U_{exp}) by filling the crater up to the original target plate level with plasticine of known density. The second method is to calculate the crater volume (U_{cal}) from the experimentally measured penetration depth (X_p) and the known variation in the projectile volume as a function of distance along its cylindrical axis from its nose tip (e.g. Fig. 1 of Ref. [24]). Thus, U_{cal} is obtained assuming that the projectile does not suffer any shape change due to plastic deformation. In contrast, U_{exp} includes not only the volume created by the projectile by penetration, but also the extra volumes created by front end spalling, by the rigid movement of the plug ahead of the projectle and by the ASB-induced micro-fracture along the crater walls (see Fig. 4). Ideally, if the projectile does not deform and if the target plate does not suffer spalling or plugging, $U_{cal}\sim U_{exp}$ and thus, as in Eqn (3), $E_{sc,cal}\sim E_{sc,exp}\sim E_{sc}$ (true). On the other hand, if the projectle deformation occurs (flattening of the nose) without any spalling or plugging of the plate, U_{exp} is the correct

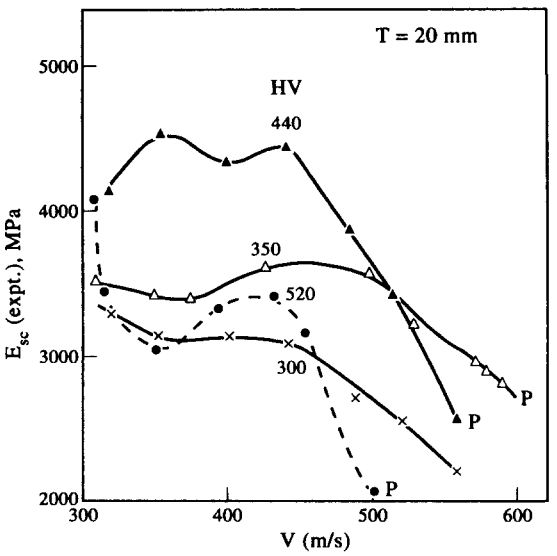

Fig. 10. The variation of the experimental cumulative specific energy absorbed per unit volume of the target material ($E_{sc,exp}$) with impact velocity for 20-mm plates of hardness HV300 (crosses), HV350 (unfilled triangles), HV440 (filled triangles) and HV520 (filled circles).

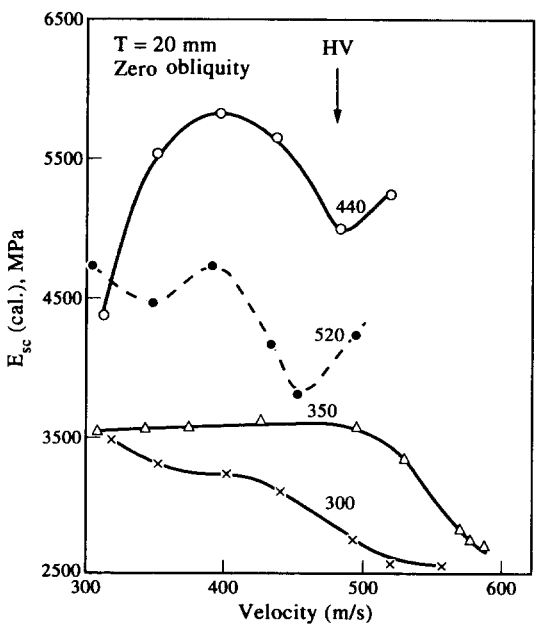

Fig. 11. The variation of the calculated cumulative specific energy absorbed per unit volume of the target material ($E_{sc,cal}$) with impact velocity for 20-mm plates of hardness HV300 (crosses), HV350 (unfilled triangles), HV440 (unfilled circles) and HV520 (filled circles).

volume while $U_{cal} < U_{exp}$. Thus, $E_{sc,exp} = E_{sc}$ (true) $< E_{sc,cal}$. In contrast, if projectile deformation does not occur but spalling/plugging of the plate occurs, U_{cal} is the correct volume and $U_{cal} < U_{exp}$. In this case, $E_{sc,cal} \sim E_s$ (true) $> E_{sc,exp}$. In conclusion, to understand the full mechanics of penetration, both $E_{sc,exp}$ and $E_{sc,cal}$ have to be estimated and compared.

The variation of $E_{sc,exp}$ and $E_{sc,cal}$ with impact velocity in the case of plates with hardness HV300, 350, 440 and 520 are illustrated in Figs 10 and 11, respectively. In terms of both $E_{sc,cal}$ and the $E_{sc,exp}$, E_{sc} values remain fairly independent of velocity. However, at higher velocities, both $E_{sc,exp}$ and $E_{sc,cal}$ start decreasing with increasing velocity. Thus the main

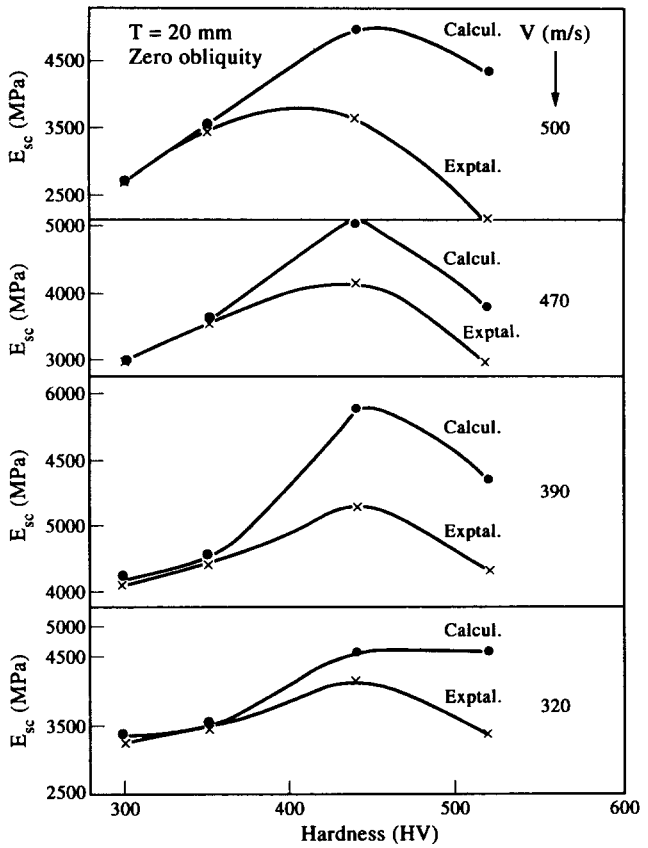

Fig. 12. The variation of $E_{sc,cal}$ and $E_{sc,exp}$ with hardness of the 20-mm plate at the constant velocities of 320, 390, 470 and 500 m s^{-1}.

point which requires emphasis is that the resistance to penetration, as characterized by E_{sc} values, is not a constant all through the penetration process. A comparison of Figs 10 and 11 also indicates that in the case of HV440 and HV520 steels, $E_{sc,cal}$ is generally higher than $E_{sc,exp}$.

To compare $E_{sc,exp}$ and $E_{sc,cal}$ values in a more critical manner and also to observe clearly the effect of hardness, the raw data in Figs 10 and 11 have been replotted in a more useful form in Fig. 12. In Fig. 12, the variation of both $E_{sc,cal}$ and $E_{sc,exp}$ with hardness of the plate is illustrated at four constant impact velocities, namely, $V = 320$, 390, 470 and 500 m s^{-1}. The most striking observation of Fig. 12 is that, irrespective of whether $E_{sc,exp}$ or $E_{sc,cal}$ is considered, E_{sc}–hardness plots go through a maximum at intermediate hardness values at all impact velocities. Thus, the energy required for perforation is lower for very high hardness plates as compared to plates with intermediate hardness. Yet another point obvious from Fig. 12 is that in the case of HV300 and HV350 plates, $E_{sc,exp} \simeq E_{sc,cal}$ at all impact velocities up to 500 m s^{-1} indicating that neither projectile deformation nor plate spalling/plugging occurred in these tests. In fact, in an earlier publication [24], it has already been demonstrated that the experimental volume of the craters formed in an HV350 plate matched very well with the penetrator volume calculated up to the depth of the penetration.

In contrast to the lower hardness plates, $E_{sc,cal} > E_{sc,exp}$ in HV440 and HV520 plates, as can be observed from Fig. 12. This difference between the experimental and calculated E_{sc} values at a given impact velocity generally increase with increasing hardness. However, at a given hardness value (HV440 or HV520), the above difference in E_{sc} values is low at $V = 320$ and 470 m s^{-1}, but high at $V = 390$ and 500 m s^{-1}. At higher hardness levels (HV440 and 520), $E_{sc,cal}$ is higher than $E_{sc,exp}$ because of both projectile deformation as well as target front end spalling/plugging. This aspect will be discussed in greater detail in Section 4.

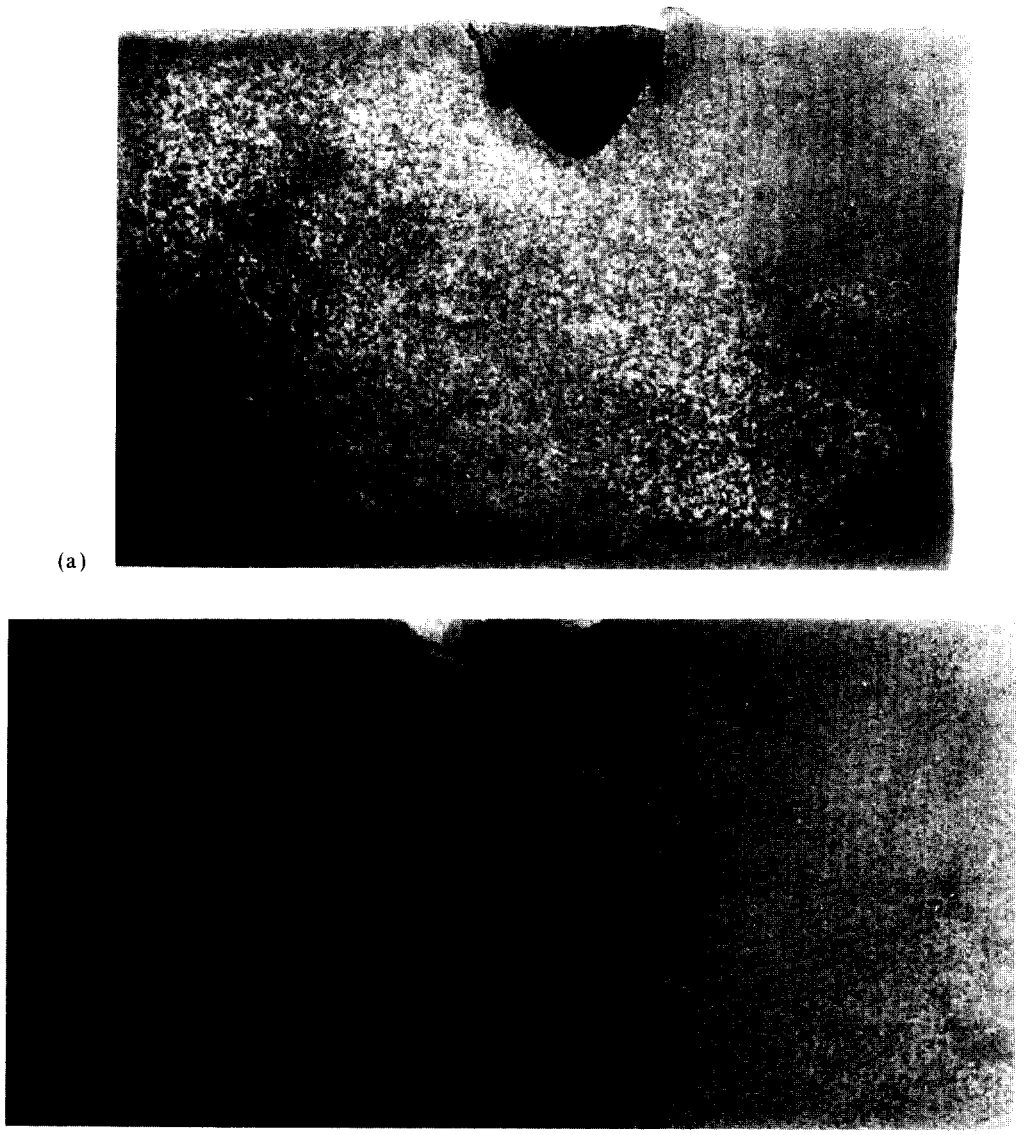

(a)

(b)

Fig. 13. Sectioned views of the craters formed on 80-mm plate of hardness HV440 and HV520 (a, HV440, $V = 789\ \mathrm{m\ s^{-1}}$; b, HV520, $V = 763\ \mathrm{m\ s^{-1}}$).

3.2. *Ballistic penetration of 80 mm plates*

(a) Appearance of impacted plates. The impacted steel plates 80 mm thick and of hardness HV295, 440 and 520 were examined for assessing the mode of deformation of the plate material. Even at the highest impact velocity, the depth of penetration was substantially smaller than the plate thickness (=80 mm) and hence only the entry sides of the plates were examined. Figures 13a and b illustrate the section view of the craters formed on HV440 ($V = 789\ \mathrm{m\ s^{-1}}$) and HV520 ($V = 763\ \mathrm{m\ s^{-1}}$) plates, respectively. The depth of penetration (X_p) in the case of HV440 plate is only about 1/4 the thickness of the plate, while in the case of HV520 plate X_p is even lower, even at the highest impact velocities. Thus, the 80-mm plate can be safely assumed to be semi-infinite as far as the penetration process is considered. In addition, it can be easily noted from Figs 13a and b that the crater profile is very shallow and quite different from the ogive profile of the penetrator nose, especially in the case of HV520 plate. Thus, a substantial deformation and flattening of the penetrator nose has occurred during the penetration process. On the other hand,

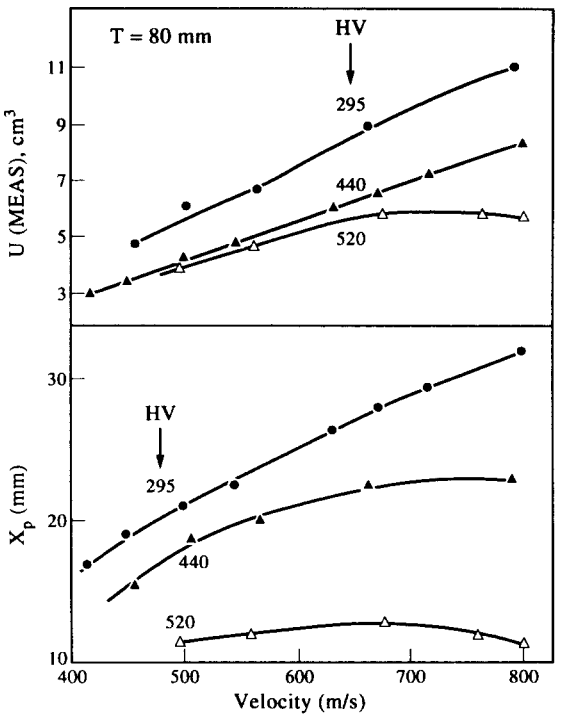

Fig. 14. The variation of depth of penetration (X_p) and experimental crater volume (U) with impact velocity for 80-mm plate of hardness HV295 (filled circles), HV440 (filled triangles) and HV520 (unfilled triangles).

in the case of HV295 plate, the projectile was largely undeformed and the crater profile was identical to that of the projectile [24].

(b) Penetration depth and volume. The variation of the penetration depth (X_p) and the crater volume (U), measured experimentally using plasticine as a function of impact velocity, are presented in Figs 14a and b respectively for 80-mm-thick steel plates of hardness HV295, 440 and 520. X_p increases monotonically with velocity (U) in the case of HV295 plate. The $X_p - V$ curve appears to saturate towards a constant value at higher velocities in the HV440 plate, while in the HV520 plate, X_p increases marginally with increasing V at low velocities but actually decreases with V at higher velocities. The crater volume (U) increases with increasing V in HV295 and 440 plates while in the HV520 plate, at higher velocities, U tends to remain constant. From Figs 14a and b it is also clear that at a given impact velocity, both X_p and U decrease with increasing hardness of the plate.

(c) The extent of plastic zone. The experimental hardness–distance profiles obtained around the impact craters formed on 80-mm plates of hardness HV295 ($V = 715$ m s^{-1}; $X_p = 29.5$ mm), HV440 ($V = 789$ m s^{-1}; $X_p = 23$ mm) and HV520 ($V = 762$ m s^{-1}; $X_p = 12$ mm) are presented in Figs. 15a, b and c, respectively. Hardness profiles were obtained at distances of 5.5 mm, 17.5 mm and 30.5 mm, 6.5 mm and 23 mm, and 9 mm and 10.5 mm from the original top surfaces of the plate in HV295, HV440 and HV520 steel, respectively. All the hardness values were normalized by the base hardness of the plate and only these normalized values are presented in Fig. 15.

It is clear from Fig. 15 that, as the crater wall is approached, the normalized hardness value initially increases from its base value of 1.0. However, in the HV440 and 520 steels, very close to the crater wall (<4 mm in HV440 steel and <2 mm in HV520 steel), the normalized hardness value decreases as the crater wall is approached, leading to a peak value of the normalized hardness at some intermediate distance from the crater wall. In contrast, in the HV295 steel, the hardness value continuously increases as the crater wall is approached. These observations can be rationalized in the same manner as in Section

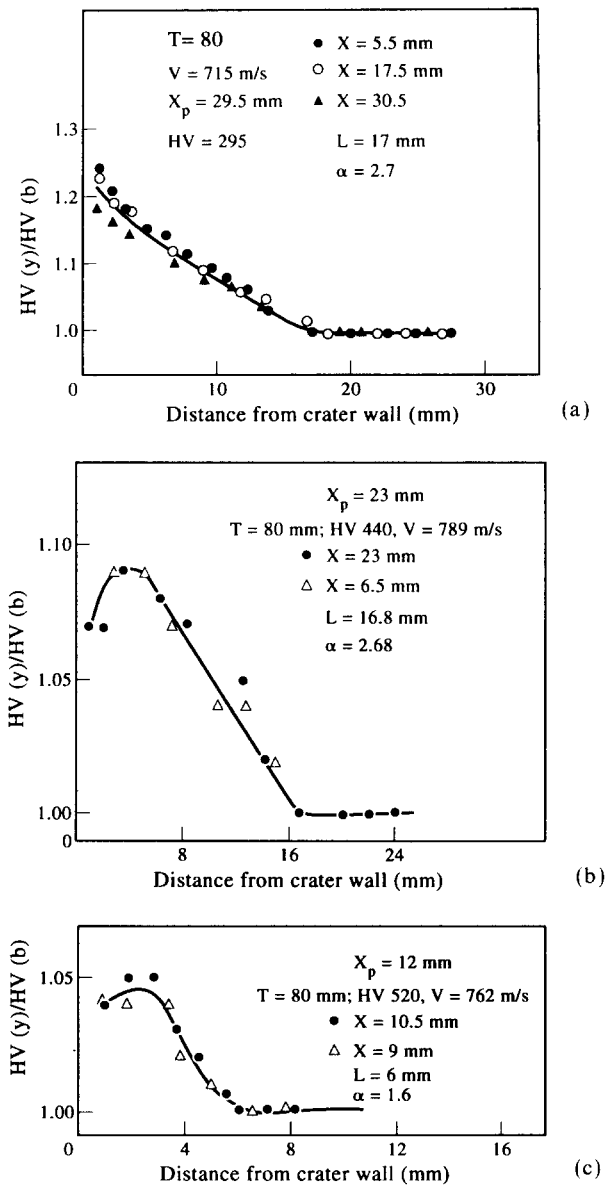

Fig. 15. The variation of normalized hardness as a function of distance from the crater wall (along the lines Y_1, Y_2 etc. illustrated in Fig. 2a) for 80-mm plates of hardness (a) HV295 ($V = 715$ m s^{-1}), (b) HV440 ($V = 789$ m s^{-1}) and (c) HV520 ($V = 762$ m s^{-1}). X represents the distance of the line along which the hardness measurements were made from the original top surface of the plate.

3.1 f. Figure 15 also indicates that the plastic zone extends to a depth (L) of 17.0, 16.8 and 5.8 mm in the case of HV295, HV440 and HV520 plates, respectively. The above values of L correspond to α value of 2.7, 2.68 and 1.58 for HV295, HV440 and HV520 steels, respectively.

(d) Cumulative specific energy absorbed. The cumulative specific energy (E_{sc}) absorbed by the 80-mm-thick plate during projectile penetration is given by Eqn (3). Further, as noted earlier, depending on whether the crater volume (U) is experimentally measured or calculated on the basis of the depth of penetration, $E_{sc,exp}$ and $E_{sc,cal}$ values can be obtained.

The variation of $E_{sc,exp}$ and $E_{sc,cal}$ with impact velocity for 80-mm-thick steel plates of hardness HV295, HV440 and HV520 are presented in Figs 16 and 17, respectively. Both $E_{sc,exp}$ and $E_{sc,cal}$ values show a general tendency to increase with increasing impact velocity. $E_{sc,cal}$ increases with increasing hardness of the plate (at a given impact velocity). In contrast, $E_{sc,exp}$ is the lowest for the HV440 steel and not the HV295 steel. Another interesting aspect to be noted from Figs 16 and 17 concerns the HV520 steel for which $E_{sc,cal}$ is considerably

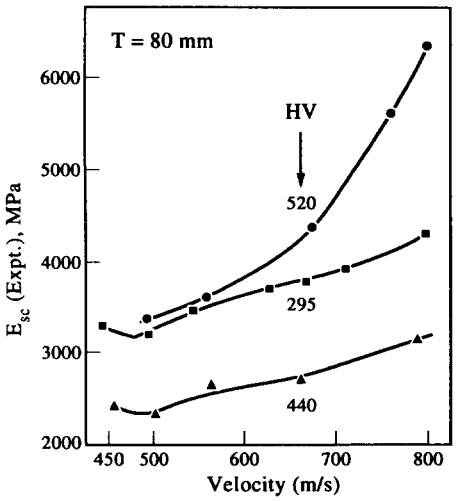

Fig. 16. The variation of $E_{sc,exp}$ with impact velocity for 80-mm plates of hardness HV295 (filled squares), HV440 (filled triangles) and HV520 (filled circles).

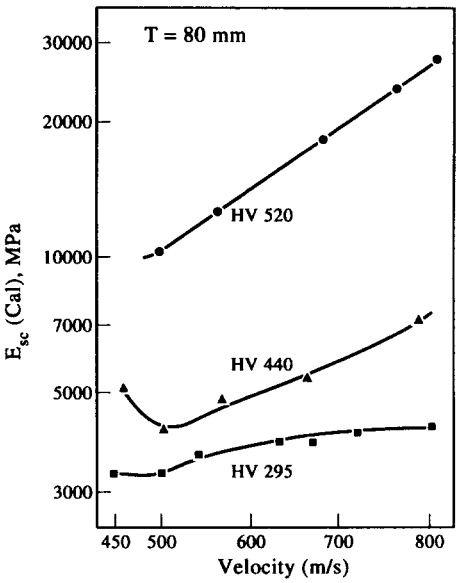

Fig. 17. The variation of $E_{sc,cal}$ with impact velocity for 80-mm plates of hardness HV295 (filled squares), HV440 (filled triangles) and HV520 (filled circles). Note the logarithmic scale employed for $E_{sc,cal}$.

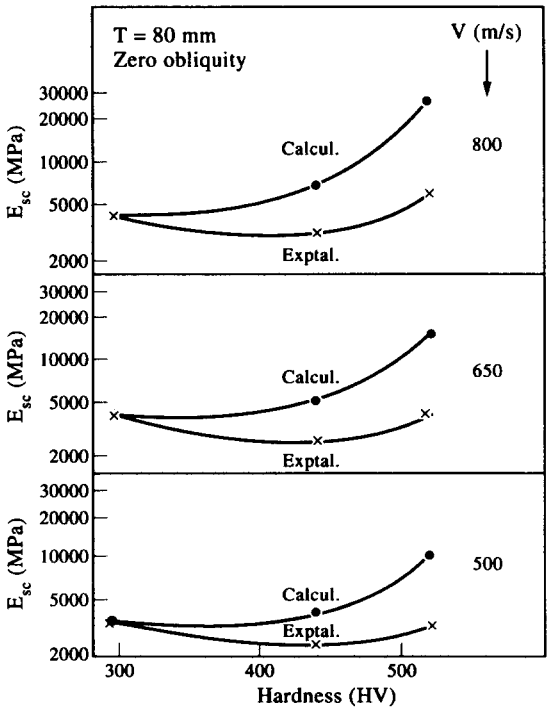

Fig. 18. The variation of $E_{sc,exp}$ and $E_{sc,cal}$ with the hardness of the 80-mm plate at three constant velocities ($V = 500$, 650 and 800 m s^{-1}).

higher than the $E_{sc,exp}$ values. In Fig. 18, the variation of $E_{sc,exp}$ and $E_{sc,cal}$ with the plate hardness is illustrated for three constant impact velocities ($V = 500$, 650 and 800 m s^{-1}). The logarithmic nature of the E_{sc} scale in Fig. 18 is to be noted. In the case of HV295 plate, $E_{sc,cal}$ and $E_{sc,exp}$ are essentially equal. However, with increasing hardness of the plate (i.e. HV440 and HV520 steels), the difference between $E_{sc,cal}$ and $E_{sc,exp}$ keeps increasing.

It is also clear from Figs 16–18 that the variation of E_{sc} (exp or cal) with impact velocity or hardness in the case of 80-mm plate is quite different from the behaviour observed in 20-mm plates (Figs 10–12).

3.3. *Summary*

The experimental results pertaining to the ballistic penetration of 20- and 80-mm-thick steel plates of varying hardness by a 20-mm ogive projectile has been described in great detail in this section. The most important of these results can be summarized as follows.

(a) In the 20-mm-thick plates, as long as the plastic zone surrounding the penetrating projectile is confined (i.e. plane strain), penetration occurs by ductile hole formation characterized by the "flow back" of the material displaced by the penetrator. In this regime, the projectile is essentially undeformed when it penetrates steel plates of hardness HV300 and HV350 as indicated by the fact that $E_{sc,cal}$ and $E_{sc,exp}$ are equal within the experimental scatter. In contrast, the projectile undergoes substantial deformation as indicated by the fact that $E_{sc,cal} > E_{sc,exp}$, when it penetrates steel plates of hardness HV440 and HV520.

(b) Once the penetrator has penetrated sufficiently for the plastic zone in the steel plate surrounding the penetrator to impinge on its backface, the deformation is no longer confined (i.e. plane stress) and the bulging phase of penetration is initiated. In the HV300 and 350 steel plates of thickness 20 mm, extensive bulging occurs and the formation of a star crack limits the extent of bulging. In contrast, in 20-mm-thick plates of hardness HV440 and 520, bulging is quite limited and cut short by plug failure.

(c) In the HV440 and 520 steel plates (thickness = 20 mm), unambiguous evidence for the presence of ASBs around and ahead of the impact crater has been obtained. Thus, it is clear that the formation of ASBs ahead of the projectile and crack propagation within these bands is responsible for plug failure.

(d) In the 80-mm plates, even at the highest impact velocities, the plastic zone ahead of the penetrating projectile is very well confined within the plate leading to penetration by plane strain, ductile hole formation. In the HV295 plate, the projectile is undeformed while it penetrates the plate. In contrast, in the HV440 and 520 plates of thickness 80 mm, the projectile undergoes substantial plastic deformation (and shape change) while penetrating the plate. In addition, the plate material around the crater periphery including the lip is removed during pentration by front end spalling. As a result, $E_{sc,cal}$ is substantially larger than $E_{sc,exp}$ in 80-mm plates of hardness HV440 and 520 as compared with 20-mm plates of equivalent hardness.

(e) The variation of the cumulative specific energy absorbed (E_{sc}) by the plate material during penetration with impact velocity follows different trends in 20- and 80-mm-thick plates. In the case of 20-mm plates, the value of E_{sc} is approximately independent of velocity at low velocities but starts decreasing with increasing velocity at the higher velocities. In contrast, in the 80-mm plates, E_{sc} generally increases with increasing impact velocity.

(f) The critical velocity for failure by plugging in the case of 20-mm plates increases with decreasing hardness of the plate. The critical velocities for plugging equal 410 m s^{-1}, 480 m s^{-1} and 600 m s^{-1} for plates of hardness HV520, HV440 and HV350, respectively.

4. DISCUSSION

4.1. *Penetration behaviour in low-hardness plates*

In the case of 20-mm-thick plates of hardness HV300 and HV350 and 80-mm-thick plates of hardness HV295, the experimental results clearly indicate that the projectile undergoes negligible deformation during its penetration in these steels and further that neither plugging nor front end spalling occurs in these plates. As a result, a model which assumes the projectile to be rigid and non-deforming while it penetrates the steel should be applicable. Such an energy-based model which assumes a depth-dependent plastic zone size (i.e. $\alpha = f(X_p)$), a velocity-dependent coefficient of friction between the projectile and the target plate and an average strain of 20% in the plastic zone, has already been proposed by the authors in an earlier publication [24]. This model also accounts for the bulging

phase assumed to initiate at the point of time when the plastic zone in the plate material ahead of the projectile impinges on the backface of the plate, by considering not only the plastic energy consumed in bending and stretching the plate material ahead of the projectile but also the inertial energy consumed in accelerating the plate material ahead of the projectile to the required velocity. It has already been demonstrated that all of the experimental results pertinent to the penetration of 20-mm-thick plates of hardness HV350 and 80-mm-thick plates of hardness HV295 can be very well rationalized on the basis of the proposed model [24]. Further, it is very easy to demonstrate that the penetration data pertaining to 20-mm-thick plates of hardness HV300 presented in the last section can also be explained using the same model if the values of K_{od} and n relevant to the plate of hardness HV300 are taken from Fig. 1.

4.2. *Penetration behaviour in high-hardness plates*

In the case of the penetration behaviour of HV440 and HV520 plates (20 and 80 mm thickness), the model described above is not valid for the following reasons.

(a) Earlier studies [24,32] have indicated that the projectile will suffer negligible deformation during its penetration into a plate if its hardness is at least 1.5 times that of the plate. On this basis, the projectile should undergo deformation while penetrating the HV440 and 520 plates, since its hardness is only HV600 as noted earlier. The present experimental data indicating that $E_{sc,cal} > E_{sc,exp}$ in both HV440 and HV520 plates (see Figs 12 and 18) also substantiates the view point that the projectile has undergone deformation. Finally, the profiles of the craters as observed on sectioned and polished plates also indicate that the nose of the projectile has flattened (e.g. compare Figs 4a and b with 4e and f; Fig. 13) especially in the 80-mm plates (Fig. 13). Thus, the assumption of a non-deforming projectile, will not be valid for HV440 and HV520 plates.

(b) High hardness plates are prone to formation of adiabatic shear bands (ASBs) under ballistic penetration conditions. Cracks propagate along these bands resulting in plugging of the plate material ahead of the projectile (see Figs 4b and d), spalling of plate material around the crater periphery on the entry side (see Figs 3 and 4, Fig. 13) and also microspalling along the crater bottom and side walls (see Figs 4, 6b and 13a and b). The model proposed earlier [24] does not take into account ASB-induced plugging and spalling of plate material.

For the two reasons stated above, the model proposed earlier and validated for low hardness plates, cannot be applied in the present case.

(a) Relative dominance of projectile deformation and plugging/spalling effects. The cumulative specific energy absorbed (E_{sc}) is a convenient parameter which can be utilized to assess the relative importance of the above two effects. As noted earlier, E_{sc} can be calculated using the experimentally measured crater volume ($E_{sc,exp}$) or using the volume calculated on the basis of the experimental depth of penetration ($E_{sc,cal}$) and, further, $E_{sc,cal}$ will be greater than $E_{sc,exp}$ irrespective of whether projectile deformation or plugging/spalling of the plate occurs. Thus, the ratio $E_{sc,cal}/E_{sc,exp}$ appears to be a useful parameter. The variation of the above ratio with impact velocity is illustrated for 20-mm-thick plates (HV300, 350, 440 and 520) and 80-mm-thick plates (HV295, 440 and 520) in Figs 19a and b respectively.

In the case of the 20-mm plate of hardness HV440 and HV520, the ratio $E_{sc,cal}/E_{sc,exp}$ initially increases with velocity (region I), reaches a maximum and then decreases to a minimum (region II) and finally increases with increasing velocity again (region III). The nature of the penetration mechanism leading to such a complex variation of $E_{sc,cal}/E_{sc,exp}$ can be understood as follows. In region I, penetration occurs by ductile hole formation under constrained, plane strain deformation conditions. However, the projectile deformation increases in extent with penetration and in addition, some material along the periphery of the crater (on the front side) is also lost by spallation. Both these processes cause the ratio $E_{sc,cal}/E_{sc,exp}$ to increase with increasing penetration or equivalently with increasing initial velocity.

However, once the plastic zone in the plate material ahead of the projectile impinges on the backface of the plate, the bulging process involving deformation under unconstrained,

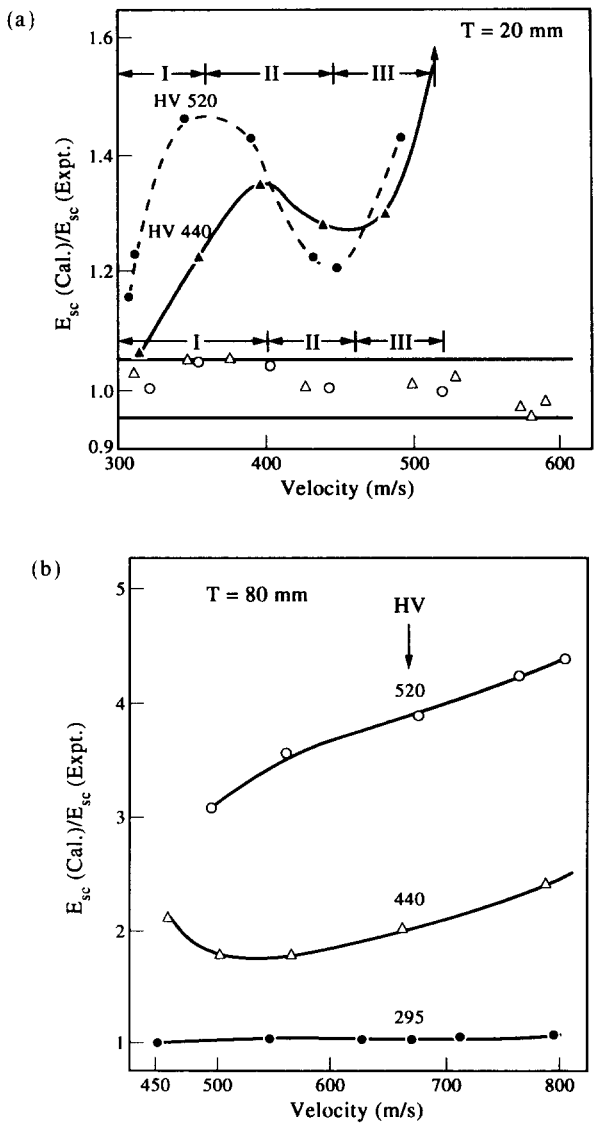

Fig. 19. The variation of the ratio $E_{sc,cal}/E_{sc,exp}$ with impact velocity for (a) 20-mm plates of hardness HV300 (unfilled circles), HV350 (unfilled triangles), HV440 (filled triangles) and HV520 (filled circles) and (b) 80-mm plates of hardness HV295 (filled squares), HV440 (unfilled triangles) and HV520 (unfilled circles). The regions I, II and III in Fig. 19a are explained in the text.

plane stress conditions is initiated. The plastic flow component of the resistance to plate penetration experienced by the projectile, decreases dramatically by a factor of almost 3 when the stress state changes from plane strain to plane stress. Thus, the projectile does not experience sufficiently high stress any longer to undergo deformation. The absence of projectile deformation in conjuction with bulging causes the ratio $E_{sc,cal}/E_{sc,exp}$ to decrease towards 1 leading to region II.

After a certain amount of bulging has occurred, ASB-induced shear plugging initiates leading to the rigid movement of the plug of the plate material ahead of and along with the projectile. As noted earlier, under these conditions the ratio $E_{sc,cal}/E_{sc,exp}$ once again starts increasing, since the experimental crater volume (inclusive of volume created by rigid movement of the plug) is considerably higher than the crater volume calculated on the basis of depth of penetration. This represents regime III.

In the 80-mm plate, even at the highest velocity, the depth of penetration in both HV440 and HV520 plates is such that the plastic zone is well confined. Thus, all the data presented

in Fig. 19b correspond to regime I involving penetration by ductile hole formation but with a deforming projectile. Thus, the continuous increase of the ratio $E_{sc,cal}/E_{sc,exp}$ with velocity is explained.

(b) Velocity–hardness mechanism map. Based on the foregoing discussion regarding the penetration mechanisms in a 20-mm-thick plate, a velocity–hardness map illustrated in Fig. 5 can be constructed. The line AB, as discussed earlier, separates the plugging failure regime from the other regimes. The line CFDE, in contrast, separates the bulging regime (plane stress) from the ductile hole formation (plane strain) regime. Within the ductile hole formation regime, the line FG delineates two sub-regimes, namely, ductile hole formation with and without projectile deformation.

For a plate with a given hardness value, increasing velocity also represents increasing depth of penetration. So the map also illustrates how the penetration mechanism changes with increasing depth of penetration in a 20-mm plate. For example, in the case of low hardness plates (HV350), initial penetration occurs by ductile hole formation (non-deforming projectile) followed by bulging and star crack formation. In contrast, for plates for high hardness (HV > 400 or so), the initial penetration is by ductile hole formation (deforming projectile) followed by bulging. However, after a certain amount of bulging, ASB-induced shear plugging is initiated leading to plate perforation.

(c) Bulging a pre-requisite for ASB-induced plugging. In the 20-mm plate, ASB formation beneath the crater and ASB propagation towards the rear surface of plate (a prerequisite for shear plugging) occurs only after a certain amount of bulging has occurred. This aspect is very clear from Fig. 7, wherein the plug initiation line AB is observed to lie well above the bulge initiation line CFDE. Similarly, in the case of the 80-mm plate, ASBs propagating beneath the craters towards the rear surface could not be detected even at the highest velocity. Thus, it appears that at least in the low alloy steel used in the present investigation, bulging is a prerequisite for ASB formation. Such a requirement is also broadly consistent with the analysis of Woodward and co-workers [33,34], which indicates that it will be energetically favourable for plugging to occur when the thickness of the material to be penetrated is less than the projectile diameter under which conditions bulging will anyway occur. The above analysis presupposes the presence of ASBs which will ultimately lead to plugging. However, the nucleation of ASBs requires special conditions to be met, as will be demonstrated below. More importantly, it will be shown that under plane stress conditions, as during bulging, nucleation of ASB is relatively easier.

In the classical sense, ASBs are formed in a material when its net strain hardening rate becomes zero [35]. Under high strain rate conditions, the plastic deformation is usually adiabatic in nature and hence the temperature of the deforming material increases due to conversion of plastic deformation to heat. This increase in temperature causes flow stress softening and if such a softening is sufficient to compensate for the increase in flow stress due to strain hardening, the formation of ASBs is facilitated. If the constitutive equation for plastic flow has the following form,

$$\sigma = K_{od}\varepsilon^{n}(1 - CT), \tag{4}$$

where C is the temperature coefficient of flow stress and T is the temperature of the deforming material, then the condition for ASB formation can be transformed to a critical equivalent strain (ε_c) criterion to give [35],

$$\varepsilon_c = [n\rho_t C_p/\gamma K_{od} C]^{1/n+1}. \tag{5}$$

In Eqn (5), ρ_t and C_p are the density and specific heat of the deforming plate material and γ is the fraction of plastic work that is converted to heat ($\simeq 0.9$). The variation of ε_c with hardness computed using the values of K_{od} and n from Fig. 1 and typical values of the other parameters ($\rho_t = 7860\ \text{kg m}^{-3}$; $C_p = 465\ \text{J kgk}^{-1}$ and $C = 3 \times 10^{-4}\ \text{K}^{-1}$ (Ref. [36])), is illustrated in Fig. 20 as filled circles. It is clear that ε_c for ASB formation decreases dramatically with increasing hardness.

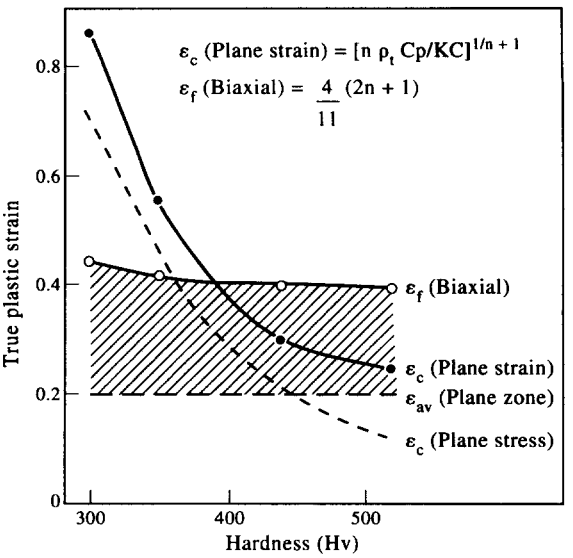

Fig. 20. The variation of the computed critical strain for ASB formation under plane strain (filled circles) and plane stress (dashed sloping line) conditions as a function of plate hardness. The unfilled circles represent the computed fracture strain for biaxial stretching induced star cracking. The shade area represents the bulge regime.

The biaxial tensile failure of the bulge resulting in star crack formation has been analysed by a number of investigators [37,38]. The most recent of these analyses is due to Woodward [38]. The equivalent strain for biaxial tensile failure (ε_f (biaxial)) is essentially related to the strain-hardening capability of the material (i.e. n in Eqn (4)) and a typical expression is given as [37].

$$\varepsilon_f(\text{biaxial}) = (4/11)(2n+1). \tag{6}$$

In Fig. 20, the unfilled circles represent the variation of ε_f(biaxial) with hardness. The variation of ε_f(biaxial) with hardness is obviously not as dramatic as in the case of ASB. It is to be noted that ε_f(biaxial) represents the strain at which the bulge will fail in biaxial tension and not the strain at which the bulge will initiate. As noted in an earlier publication [24], the average strain in the confined plastic zone is about 0.2 for an ogive-shaped projectile. This value of 0.2 should thus represent the bulge initiation strain. However, once the bulge forms, the plastic zone is no longer confined and so the plastic strain in the plastic zone starts increasing rapidly and ultimately reaches ε_f(biaxial). Thus, the shaded area in Fig. 20 represents the bulge regime.

As in Fig. 20, in the case of plane strain penetration (i.e. no bulge), ε_c for ASB formation is always greater than the average strain in the plastic zone (ε_{av}) and hence ASB formation and the attendant plugging should not occur at any hardness level. This prediction is consistent with the experimental results of 80-mm plates, where penetration occurred under plane strain conditions.

The ε_c values for ASB formation plotted in Fig. 20 (filled circles) are strictly valid only under plane strain conditions wherein the presence of a large hydrostatic compressive stress in the plastic zone effectively prevents void formation on the second phase particles (like inclusions and carbides). On the other hand, once the bulging occurs (plane stress) the plastic zone is no longer confined and, consequently, the hydrostatic compressive component is reduced substantially. Under these conditions, void nucleation is favoured on the second phase particles, as in a tensile test for example. The presence of voids, essentially strain concentrators, aids the formation and also stabilizes the formation of ASB. Dodd and Atkins [39] have modelled the formation of ASBs in the presence of voids and have demonstrated that ε_c can be substantially lower than the values predicted by Eqn (5)

under such conditions. Cowie and co-workers [40,41] have also provided substantial evidence for the destabilizing influence of the voids on ASB formation by carrying out detailed experiments under pure shear deformation conditions, illustrating the positive influence of both hydrostatic stress and inclusion content on the critical shear strain for flow instability resulting from shear band formation.

The dashed line in Fig. 20 qualitatively illustrates the fact that the ε_c for ASB can be reduced substantially once bulging characterized by plane stress is initiated. Thus, it is clear from Fig. 20 that the penetration can occur by shear plugging once bulging has just initiated in the case of very hard steels (i.e. region III in Fig. 20). This prediction is consistent with the experimental observation of such a transition from bulging to shear plugging in 20-mm-thick steel plates of hardness HV440 and 520 (see Fig. 5).

(d) Energy absorbed in shear plugging and bulging. In an earlier paper [24], an expression for the energy absorbed in bulging (E_{bul}) which also takes into account the inertial energy consumed in accelerating the plate material forming the bulge to the projectile velocity was developed. It should therefore be instructive to compare the energy absorbed in shear plugging (E_{plug}) with that absorbed in bulging (E_{bul}).

If it is assumed that the shear energy absorbed per unit volume in the ASB up to the point of fracture along the shear band is given by $(K/2)\,(\varepsilon_{fs}^{n+1}/n+1)$, where ε_{fs} is the local fracture strain in the shear band ($\simeq 1$–5), and if the width of the shear band is assumed equal to the width of the ASB observed experimentally (Fig. 6), then a simple expression for E_{sc} assuming only shear plugging as the penetration mechanism can be obtained as demonstrated elsewhere [42]. A detailed analysis of this expression using values typical of the steels clearly indicates that the energy absorbed in creating a unit volume of the crater/hole (i.e. E_{sc}) in the steel plate is two to four orders of magnitude lower for shear plugging as compared with bulging. Thus, in terms of energy absorption, only penetration by ductile hole formation and bulging needs to be considered. The effect of shear plugging on energy absorption is indirect in the sense that it terminates bulging at an early stage and thus reduces the total energy absorption levels.

(e) Critical depth of penetration for plugging. An examination of the impacted steel plates is usually enough to demarcate the plugged region, if any, since it is characterized by a shiny surface. Thus, the critical depth of penetration (X_{pc}) defined as the depth at which the shear plug initiated during penetration, could be easily determined. Table 2 gives the values of X_{pc} and X_{pc}/T (T=plate thickness) obtained from impacted 20-mm-thick plates of hardness HV440, 470 and 520. It is clear from Table 2 that X_{pc}/T is nearly a constant ($\simeq 0.58 \pm 0.08$) independent of plate hardness and impact velocity. Since only one type of projectile of diameter (D) 20 mm was used throughout the present work, the data in Table 2 imply that X_{pc}/D is also nearly a constant ($\simeq 0.58 \pm 0.08$).

A constant value of X_{pc}/D is consistent with the prediction of the model due to Woodward [33]. The model, however, predicts a value of 0.86 for X_{pc}/D which is some what higher than the experimental value of 0.58 ($\simeq 0.08$). An alternative approach based on the analysis presented in Section 4c is to assume that the plastic zone should impinge on the backface of the plate for ASB to form and hence plugging to occur. On the basis of this approach, X_{pc} should equal $T-L$ (L=plastic zone thickness ahead of the projectile). Our continuing work on the study of the penetration behaviour of steel plates of thickness 10, 20, 40 and 80 mm by projectiles of diameter 6.2, 20, 40 and 60 mm has clearly shown that L is primarily a function of depth of penetration (X_p) and only marginally influenced by other parameters [42]. Such a proportionality between L and X_p (i.e. $L=Q.X_p$) transforms the relation $X_{pc} \simeq T-L$ to $X_{pc}/T \simeq 1/(1+Q) \simeq$ constant. Our preliminary analysis of L vs X_p data suggests a value of 0.65 for Q [42]. With this value of Q, X_{pc}/T equals 0.6, a value consistent with the experimental data (Table 2).

(f) The effect of plate hardness. The effect of plate hardness on ballistic penetration depends very much on the stress state accompanying the penetration. Under plane strain conditions, wherein the plastic zone is confined, the harder the material the greater is the resistance to ballistic deformation. This comes about because of the higher energy dissipated in the plastic zone with increasing hardness and also because of the blunting of the

projectiles. In contrast, under plane stress conditions, the effect of hardness on ballistic penetration is dramatically different. At higher hardnesses of the plate, beyond HV440 or so, ASB-induced shear plugging limits the penetration resistance while at very low hardnesses, the energy dissipated in the plastic zone is very low leading to low resistance again. As a result the maximum resistance to penetration occurs at an intermediate hardness. Such a contrasting effect of hardness on ballistic penetration under plane strain and plane stress provides the rationale for the well-known fact that a steel plate with graded hardness will out-perform homogeneous steel plates with one hardness value. For example, a steel plate with a high hardness on its front face but with a negative hardness gradient along thickness direction will certainly exhibit improved resistance to ballistic penetration.

(g) The effect of plate thickness. The present work clearly indicates the effect of plate thickness on ballistic penetration is not straightforward. At one extreme, in the case of very hard steel plates (>HV500), the effective thickness of the plate just equals $0.6T$ (T=nominal thickness) as noted earlier. In contrast, in the case of low hardness plates (<HV350), up to a thickness of $0.6T$, the resistance to penetration is high as characterized by the plane strain, constrained value of E_{sc}. However, over the penetration range of $0.6T$ to $(1.2\text{–}1.4)T$ (the extract maximum value depending on the extent of the bulge), though E_{sc} value is about half the earlier value because of unconstrained plane stress conditions, it is not negligible. Thus, the effective thickness lies in the range 0.9 to $0.95T$ under these conditions.

As a first approximation, the resistance offered by a plate of effective thickness T_e is given by (HV). T_e (HV is the hardness of the plate). Thus the resistance per unit area offered by the plates of hardness HV500 ($T_e=0.6$), HV400 ($T_e=0.9$ for bulge height of $0.2T$) and HV300 ($T_e=1.00$ for bulge height of $0.4T$) equal 3000, 3600 and 3000 MPa, respectively. However, the above statement is valid only if the plates are perforated during penetration. If the thickness of the plates are such that the depth of penetration never exceeds $0.6T$ or so, then the resistance provided by the plate to ballistic penetration scales in the same way as its hardness.

5. CONCLUSIONS

(1) The effect of hardness of a plate on ballistic performance depends on whether the stress state is predominantly plane strain or plane stress.

(2) Under plane strain conditions (i.e. 80-mm plate), increasing the hardness of the plate increases the resistance to penetration. This increased resistance is due to the increased energy dissipated in the plastic zone formed in the plate around the projectile with increasing hardness (strength) and also due to the increase in the extent of deformation of the projectile with increasing hardness of the plate.

(3) Under plane stress conditions (i.e. 20-mm plate), as the hardness of the plate increases, the resistance to penetration also increases initially. But beyond a hardness of HV440 or so, any further increase in the hardness of the plate actually decreases its resistance to penetration due to the onset of adiabatic shear band induced plugging. Thus, under plane stress conditions (i.e. 20-mm plate), the resistance of the plate to ballistic penetration is maximum at intermediate hardness levels.

(4) Adiabatic shear band (ASB) formation and hence the plugging mode of failure occurs only under plane stess conditions in the low alloy steel used in the present investigation. This result implies that the softening of the material caused by void nucleation may be a necessary precursor to ASB formation.

Acknowledgements—The authors wish to express their gratitude to the Director, DMRL, for granting permission to publish this paper.

REFERENCES

1. W. Johnson, *Impact Strength of Materials*. Edward Arnold, London (1972).
2. M. E. Backman and W. Goldsmith, The mechanics of penetration of projectiles into targets. *Int. J. Engng Sci.* **16**, 1–99 (1978).
3. E. W. Billington and A. Tate, *The Physics of Deformation and Flow*, Chap. 13. McGraw-Hill, New York (1982).
4. C. E. Anderson and S. R. Bodner, Ballistic impact: The status of analytical and numerical modelling. *Int. J. Impact Engng* **7**, 9–35 (1988).
5. G. I. Taylor, The formation and enlargement of a circular hole in a thin plastic sheet. *Q. J. Mech. Appl. Math.* **1**, 103–124 (1948).
6. W. T. Thompson, An approximate theory of armour penetration. *J. Appl. Phys.* **26**, 80–82 (1955).
7. C. A. Calder and W. Goldsmith, Plastic deformation and perforation of thin plates resulting from projectile impact. *Int. J. Solids Struct.* **7**, 863–881 (1971).
8. A. I. O. Zaid and F. W. Travis, Conference on mechanical properties at high rates of strain. *Conference Series* No. 21 (Edited by J. Harding), pp. 417–428. Institute of Physics, London (1974).
9. J. W. Lethaby and I. C. Skidmore, The deformation and plugging of thin plates by projectile impact. *Inst. Phys. Conf. Ser.* **21**, 429–441 (1974).
10. J. Liss. W. Goldsmith and J. M. Kelly, A phenomelogical penetration model for thin plates. *Int. J. Impact Engng* **1**, 321–341 (1983).
11. R. S. J. Corran, P. J. Shadbolt and C. Ruiz, Impact loading of plates—An experimental investigation. *Int. J. Impact Engng* **1**, 3–22 (1983).
12. P. J. Shadbolt, R. S. J. Corran and C. Ruiz, A comparison of plate perforation models at sub-ordnance impact velocity range. *Int. J. Impact Engng* **1**, 23–50 (1983).
13. N. Levy and W. Goldsmith, Normal impact and perforation of thin plates by hemispherically-tipped projectiles—1. Analytical considerations. *Int. J. Impact Engng* **2**, 209–229 (1984).
14. N. Levy and W. Goldsmith, Normal impact and perforation of thin plates by hemispherically tipped projectiles—II. Experimental results. *Int. J. Impact Engng* **2**, 229–324 (1984).
15. B. L. Landuof and W. Goldsmith, Petalling of thin metallic plates during penetration by cylindro-conical projectiles. *Int. J. Solids Struct.* **21**, 245–266 (1985).
16. W. Goldsmith, Initiation of perforation in thin plates by projectiles. In *Metal Forming and Impact Mechanics* (Edited by S. R. Reid), pp. 271–288. Pergamon Press, Oxford (1985).
17. R. L. Woodward, A structural model for thin plate perforation by normal impact of blunt projectiles. *Int. J. Impact Engng* **6**, 129–140 (1987).
18. C. Palomby and W. Stronge, Blunt missile perforation of thin plates and shells by discing. *Int. J. Impact Engng* **7**, 85–100 (1988).
19. R. G. Teeling-Smith and G. N. Nurick, The deformation and tearing of thin circular plates subjective to impulsive loads. *Int. J. Impact Engng* **11**, 77–91 (1991).
20. J A. Zukas, T. Nicholas, H. F. Swift, L. B. Greszczuk and D. R. Curran (Editor), *Impact Dynamics*. John Wiley, New York (1982).
21. W. Goldsmith and S. A. Finnegan, Normal and oblique impact of cylindro-conical and cylindrical projectiles on metallic plates. *Int. J. Impact Engng* **4**, 83–105 (1986).
22. R. L. Woodward, Penetration of semi-infinite metal targets by deforming projectiles. *Int. J. Mech. Sci.* **24**, 73–87 (1982).
23. G. Sundararajan and P. G. Shewmon, The oblique impact of a hard ball against ductile, semi-infinite target materials—experiment and analysis. *Int. J. Impact Engng* **6**, 3–22 (1987).
24. S. N. Dikshit and G. Sundararajan, The penetration of thick steel plates by ogive shaped projectiles—experiment and analysis. *Int. J. Impact Engng* **12**, 373–408 (1992).
25. J. Awerbuch and S. R. Bodner, Analysis of mechanics of perforation of projectiles in metallic plates. *Int. J. Solids Struct.* **10**, 671–684 (1974).
26. M. Ravid and S. R. Bodner, Dynamic perforation of viscoplastic plates by rigid projectiles. *Int. J. Engng Sci.* **21**, 577–591 (1983).
27. J. Dehn, A unified theory of penetration. *Int. J. Impact Engng* **5**, 239–248 (1987).
28. R. C. Batra, Steady state penetration of viscoplastic target. *Int. J. Engng Sci.* **25**, 1131–1141 (1987).
29. A. L. Wingrove and G. L. Wulf, Some aspects of target and projectile properties on penetration behaviour. *J. Aust. Inst. Metals* **18**, 167–173 (1973).
30. J. Manganello and K. H. Abbott, Metallurgical factors affecting the ballistic behaviour of steel targets. *J. Materials, JMLSA* **7**, 231–239 (1972).
31. R. L. Woodward, The interrelation of failure modes observed in the penetration of metallic targets. *Int. J. Impact Engng* **2**, 121–129 (1984).
32. Y. Tirupataiah and G. Sundararajan, The volume of the crater formed by the impact of a ball against flat target materials—The effect of ball hardness and density. *Int. J. Impact Engng* **9**, 237–246 (1990).
33. R. L. Woodward, The penetration of metal targets which fail by adiabatic shear plugging. *Int. J. Mech. Sci.* **20**, 599–607 (1978).
34. R. L. Woodward, B. J. Baxter and N. V.Y. Scarlett, Mechanisms of adiabatic shear plugging failure in high strength aluminium and titanium alloys. *Inst. Phys. Conf. Ser.* No. 70, *Proc. 3rd Conference on Mech. Prop. of Materials at High Rates of Strain* (Edited by J. Harding), pp. 525–532. Institute of Physics, London (1984).

35. Y. Tirupataiah and G. Sundararajan, A dynamic indentation technique for the characterization of high strain rate flow behaviour of ductile materials. *J. Mech. Phys. Solids* **39**, 243–62 (1991).
36. G. Sundararajan, The correlation of erosion and wear resistance of pure metals with their mechanical and thermophysical properties. *Scripta Met.* **19**, 347–52 (1985).
37. W. Johnson and P. B. Mellor, *Plasticity for Mechanical Engineers*, p. 187. Van Nostrand, New York (1962).
38. R. L. Woodward, A simple one-dimensional approach to modelling ceramic composite armour defeat. *Int. J. Impact Engng* **9**, 455–474 (1990).
39. B. Dodd and A. G. Atkins, Flow localization in shear deformation of void-containing and void-free solids. *Acta Metall.* **31**, 9–15 (1983).
40. J. G. Cowie, M. Azrin and G. B. Olson, Microvoid formation during shear deformation of ultra high strength steels. *Metall. Trans.* **20A**, 143–153 (1989).
41. J. Cowie and Tuler, *Mat. Sci. Engng* **95**, 93–99 (1987).
42. G. Sundararajan and S. N. Dikshit, Unpublished work, DMRL, Hyderabad, India (1992).